4 SkyPlot Program Detail

The previous chapter discussed the SkyPlot program in basic terms. This chapter looks at each aspect of the program's structure in detail and describes what physical and mathematical models it employs. The pattern of discussion observes the following plan:

- structure

- equations of motion

- extra astronomical/physical effects taken into account

4.1 Dual Time Increments (Time Steps)

Before going into detail about the program, a more basic part of its structure needs to be discussed first.

Two types of time increment (time step) are used in the program. One for observing, when the debris is visible to the detector and requires a fine timestep, and one for scanning, when the debris is not visible, and only a coarser time step is required. The larger scan timesteps were introduced into the algorithm to facilitate faster run times for the program. This dual time step feature and the bisection ("homing") method of accurately finding the time of an event (see section 4.2), is a standard method for satellite prediction programs (Kelso, 1997).

While the debris is visible, the observing time steps are small enough to enable at least one position to be recorded inside every sky bin along the debris trajectory to prevent aliasing effects (Figure 4.1). The alt/az bins have a size of 2º×2º, so given a typical topocentric zenith angular velocity of ~1.5ºs^{-1} for an object in LEO, a time step of about 1s would ensure at least one recorded position for sky bins at the zenith. Failure to do so would result in some bins not being "illuminated" by the debris, even though those bins contained the trajectory (Figure 4.1). Away from the zenith the topocentric angular velocity is smaller due to foreshortening, but altering the time step size to reflect this and minimise execution time would have been too complex an undertaking. Instead the time step size is simply chosen to be that which would allow illumination of the alt/az bins at the zenith.
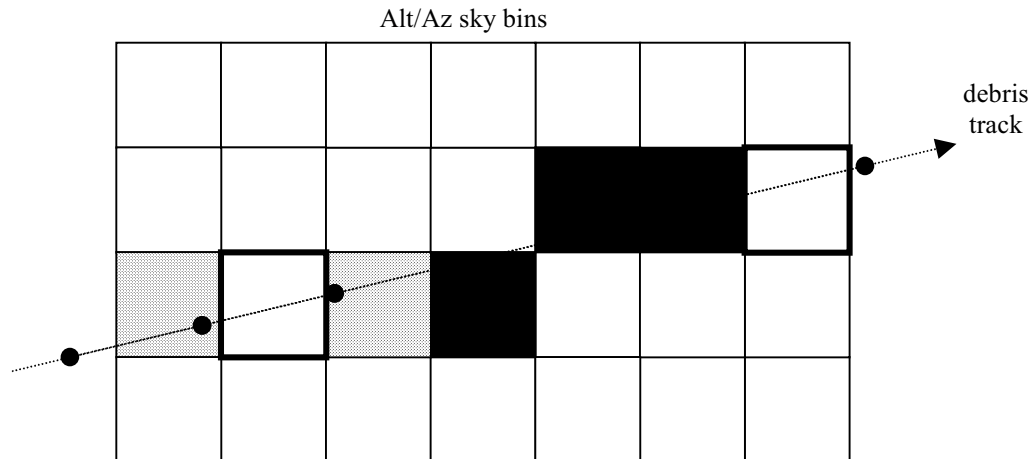
Alt/Az sky bins

Figure 4.1: Illustration of the effect of aliasing. The time steps are too large to enable all sky bins along the debris track to be "illuminated" by the debris position increments (equidistant dots along track). Illuminated sky bins are shaded, unilluminated bins along track are shown in bold.

This timestep size is unnecessary for the periods when the debris is below the horizon or within the Earth's shadow. Instead, a larger time increment is used which reduces execution time. These coarse and fine timesteps are referred to as the "scanning" and "observing" (or "scan" and "obs") timesteps respectively, and the program is referred to as being in "scan" or "obs" mode when using the appropriate timestep.

The size of the scan timestep is chosen to minimise execution time without losing accuracy. If the scan timestep is too large, short-duration apparitions, such as produced between rising and entering the Earth's shadow for example, will be missed entirely. Running the SkyPlot program with the same parameters but changing the size of the scan timestep, for debris in a Mir-type orbit observed from Mauna Kea through January-March 1998, shows this effect (Figure 4.2)

Maximum Scan Timestep

The maximum timestep for scan is dictated by the size of skybin (2° square), and the maximum angular speed of debris. The minimum length of detection scan track chosen to be two skybins. The timestep for scan mode is that of the time taken to cross two skybins; i.e.

$$t_{scan} = \frac{4^\circ}{\omega_{top}} \qquad , \qquad (4.1)$$

Apparition and Run Time Sensitivity to Scan Timestep
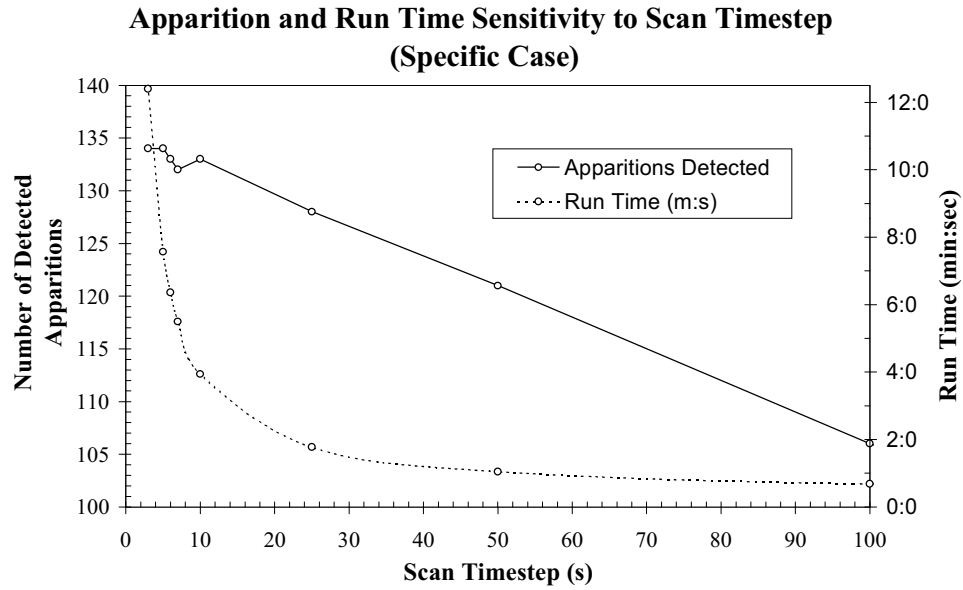**(Specific Case)**

Figure 4.2: Effect of altering scan timestep on detection rate. With finer scan timesteps, more shorter-duration apparitions are detected, until the value levels off with a sufficiently low timestep, indicating a threshold value of fineness has been reached. The dip between 5 and 10 seconds is probably caused by slightly different geometry produced by the different timesteps. Also shown is the general behaviour of run time; with finer timesteps the run time increases dramatically.

where from equation (2.25)

$$\omega_{top} = \frac{R}{h}\left[\omega_d{}^2 + (\omega_o \cos L)^2 - 2\omega_d\omega_o \cos i\right]^{\frac{1}{2}} \text{ rad s}^{-1}, \qquad (4.2)$$

where R = orbital radius (m), h = orbital height (m), ω_d = geocentric debris angular speed (rad s^{-1}), ω_o = sidereal rotation rate (7.295×10^{-5} rad s^{-1}), L = site latitude (rad), i = orbital inclination (rad).

The value of ω_{top} is overestimated by assuming i to be 90°. In this way there is no loss of accuracy as the corresponding scan time is underestimated, giving only a slight degradation of execution time. Thus equations (4.1) and (4.2) become:

$$t_{scan} = \frac{6.9813\times10^{-2} \text{ h}}{a\left[\omega_d{}^2 + (\omega_o \cos L)^2\right]^{\frac{1}{2}}} \text{ sec}, \qquad (4.3)$$

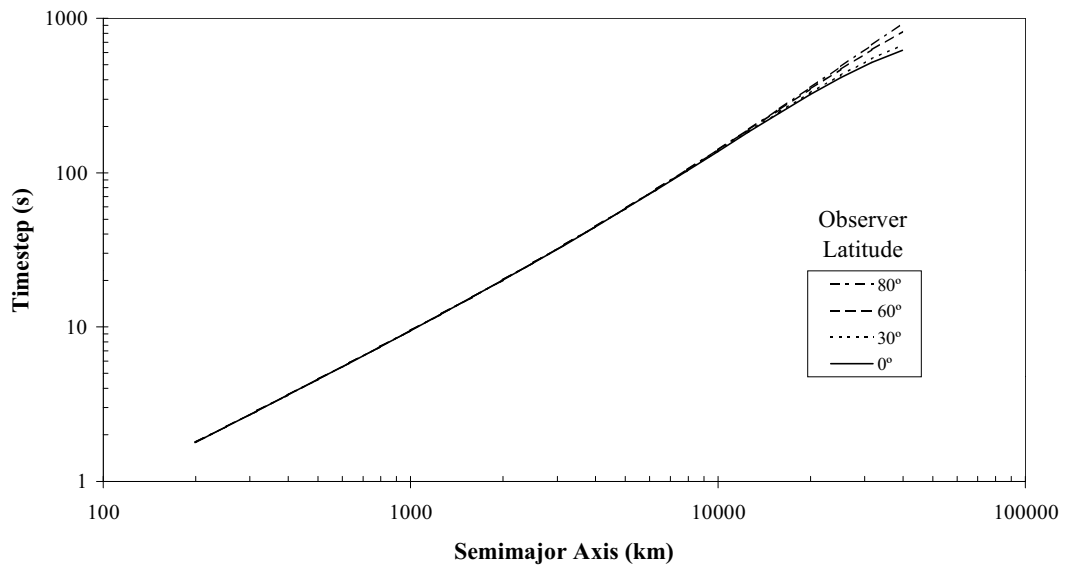a graph of which is shown in Figure 4.3.

Figure 4.3: Scan timesteps from equation (4.3) for circular orbits. It can be seen that the effect of changing latitude of observer becomes apparent for orbits above about 10000km.

4.2 Homing

The transition from scan to obs mode, if performed as a mere change of timestep, would result in the obs mode starting off where the scan mode finished. As the scan mode timestep is larger than that of the obs mode, the first obs mode position would appear removed from where it physically would appear (see Figure 4.4).
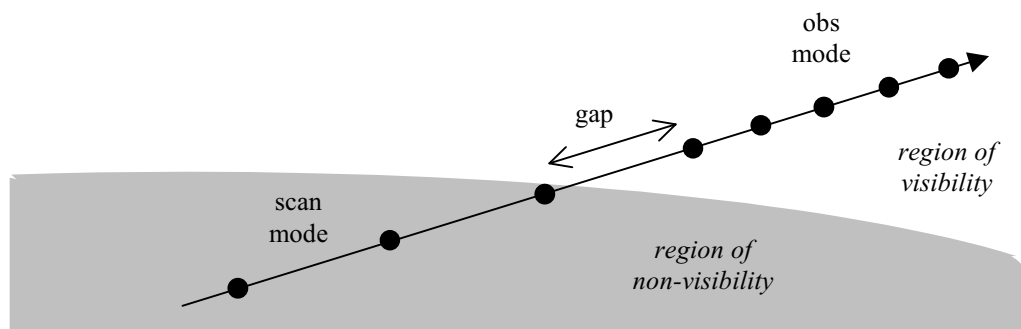

Figure 4.4: Simple transition from scan to obs mode and the resulting "Transition Gap" that arises as a result.

To avoid this problem the algorithm detects a change of mode and homes in on the mode interface, stopping when the interval between successive iterations falls below the current obs timestep. This is achieved by calculating the position vectors of the observer and debris for two successive timesteps and comparing the topocentric visibility "status" for each, assigning a value of *0* for "not visible" and *1* for "visible".

If the status is zero for both positions, the debris has not crossed the transition from "not visible" to "visible", and the program continues in scan mode. If however the second of the two positions has a visibility status of *1*, the homing loop is invoked. It follows the standard bisection technique to find the roots of a polynomial: the interval between the points containing the root is halved and each half compared to determine if the root lies within it. If not, the other half is scanned, but if so, the interval is halved again and the process repeated until the interval reaches the required accuracy (Figure 4.5).
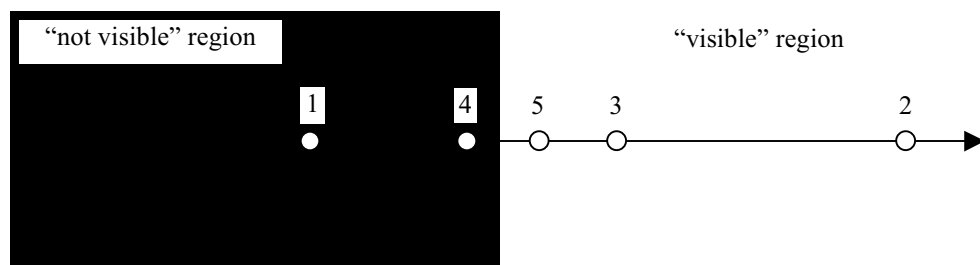

Figure 4.5: Illustration of the homing algorithm (see text).

The code used to perform these calculations is the main code in the program itself; i.e. no extra code is used. Execution flow is controlled by monitoring and comparison of the twin visibility status variables during each loop.

4.3 Coordinate system

The coordinate system used for the purposes of the SkyPlot program is a rectangular equatorial geocentric system with axes aligned with the First Point of Aries, the North Celestial Pole, and the third axis orthogonal to the first two. This places the (x,y) plane in the plane of the Earth's equator, the z axis parallel with the Earth's axis.

4.4 Equations of satellite motion

This section discusses the equations of motion of a body in a closed orbit about the Earth, and their implementation in the SkyPlot program.

4.4.1 Orbit terminology

The size and shape of an elliptical orbit is defined by its semimajor axis (a) and eccentricity (e) (Figure 4.6). The eccentricity range is $0 \leq e < 1$; zero for circular orbits, while e = 1 defines a parabolic orbit. In such a case, the orbit is not bound, i.e. it is moving at exactly escape velocity for its distance from the Earth, and barring impact with the Earth, it will leave Earth space and not return. Eccentricities greater than unity define hyperbolic orbits, which are again unbound but with higher energies. For this reason in future discussions, debris in such orbits is not considered as it poses only a fleeting hazard. LEO and GSO orbits have eccentricities approximately equal to zero, whereas GTO and Molniya orbits are very eccentric with a value of $e \sim 0.7$.

The perigee defines the point of closest approach to the Earth's surface, while the point furthest away is the apogee. Orbital velocity is greatest at perigee and least at apogee.

The orientation of the orbital plane to the coordinate system and of the orbit within the orbit plane are given by the inclination (**i**), the longitude of the ascending node (Ω), and the argument of perigee (ω) (Figure 4.7). The inclination (i) is the angle the orbital plane makes with the plane of the Earth's equator. The Longitude of the Ascending Node (Ω) is the angle around the equatorial plane between the First Point of Aries and the Ascending Node, the point where the orbit crosses the equatorial plane, heading north. This fixes the orientation of the orbital plane with respect to the geocentric coordinate system mentioned above.

The Argument of Perigee (ω) is the clockwise angle measured from the Ascending Node to the perigee, and fixes the orientation of the orbit within the orbital plane.

The final parameter is the Epoch of Perigee (τ), which fixes the satellite or debris particle along the orbit. This is a fixed time at which the particle last passed
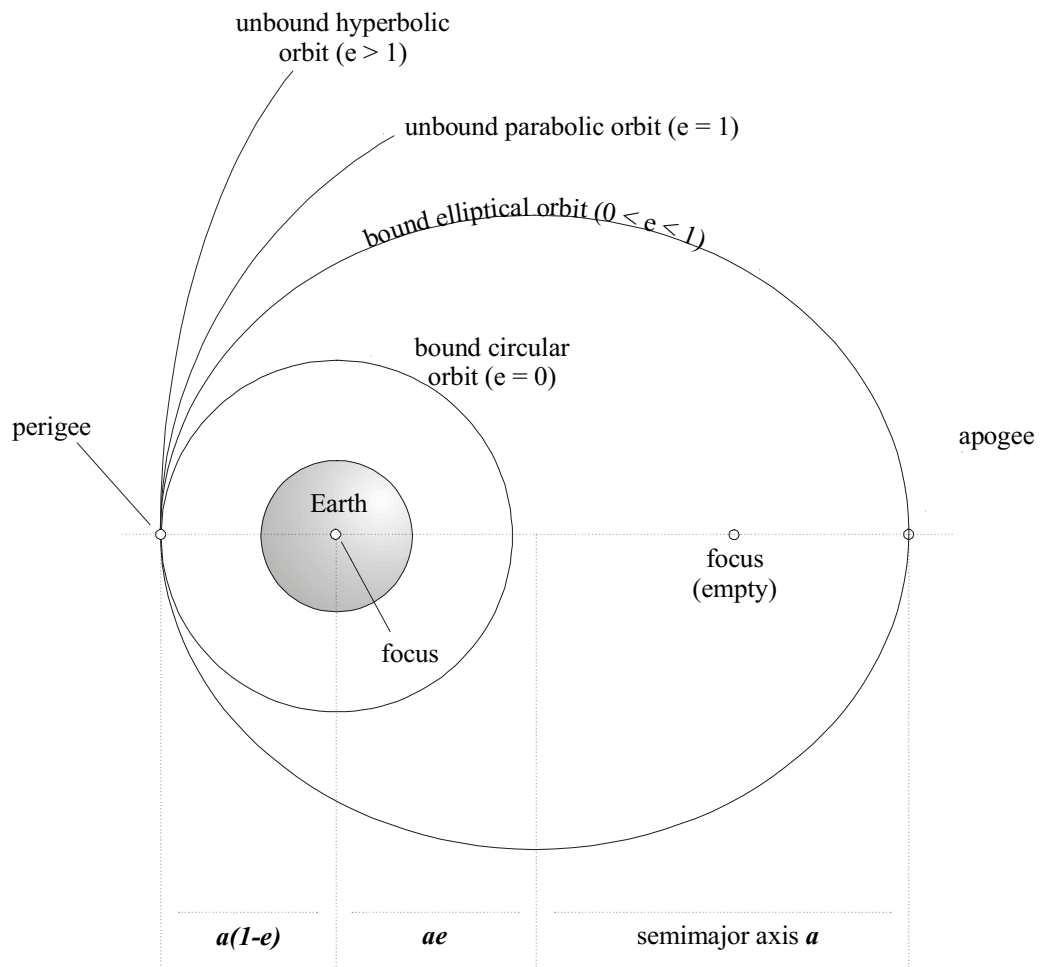
Figure 4.6: Definition of elements that determine the shape and size of an orbit within the orbital plane. Also illustrated are unbound orbits and some other measurements.

(or is due to pass) through perigee. Thus for any other time, the elapsed time since the epoch of perigee is calculated, and is then used to calculate the position of the satellite using the other orbital elements.

4.4.2 Position in the orbit

Given the orbital elements, the satellite's position anywhere in its orbit can be calculated at any time by finding its true anomaly using the following method (Roy, 1988). This is only an approximate method however, because it is derived from the simple "two-body" solution to orbital mechanics, which assumes the only force at play in the system is the radial gravitational force between the Earth and the satellite.

In real life, other forces exist which perturb the idealised motion, which are discussed in section 4.5. However, the two-body solution is a very good approximation and serves as a starting point for orbital mechanics. The mean

geocentric angular velocity of the debris, its mean motion **n**, is given by:

$$n = \left(\frac{GM_e}{a^3}\right)^{\frac{1}{2}} \quad rad\ s^{-1},$$
(4.4)

where the gravitational constant G $= 6.668 \times 10^{-11}$ N m^2 kg^{-2}, and M$_e$ = mass of Earth = 5.98×10^{24} kg. Position around the orbit is defined using the Mean Anomaly **M**, the Eccentric Anomaly **E** and the True Anomaly **f** (Figure 4.8).
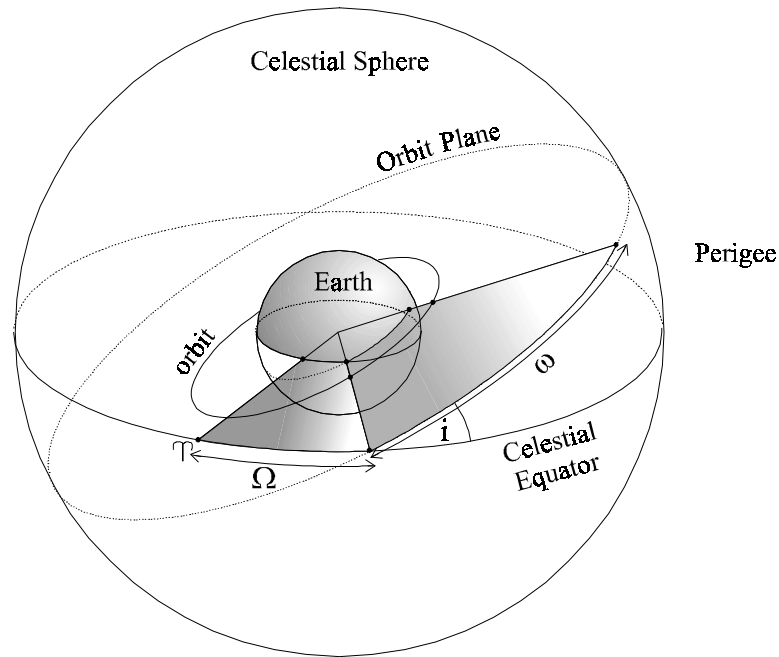

Figure 4.7: Illustration of elements of orbit orientation. The orbit itself is projected onto the celestial sphere where the pertinent angles are depicted for clarity

The mean anomaly **M** is the angle from perigee swept by a radius vector rotating with angular velocity n, so that at time t since perigee passage at τ, the mean anomaly is defined by:

$$M = n(t - \tau) \quad rad.$$
(4.5)

The eccentric anomaly **E** is related to the mean anomaly by eqn (4.6) which is known as Kepler's Equation, and which can only be calculated by iterative methods, the routine for which can be taken from e.g. Duffett-Smith (1987).

$$M = E - e\sin(E) \quad rad.$$
(4.6)

The eccentric anomaly relates to the true position of the debris by producing a line perpendicular to the major axis through the debris position to meet a circle circumscribed about the elliptical orbit (see Figure 4.8) at Q; the angle PCB is the eccentric anomaly E, as measured from the centre of the ellipse.

The true anomaly is the true angle from perigee to the debris position as measured from the focus (see Figure 4.8), and is related to the eccentric anomaly by the following equation:
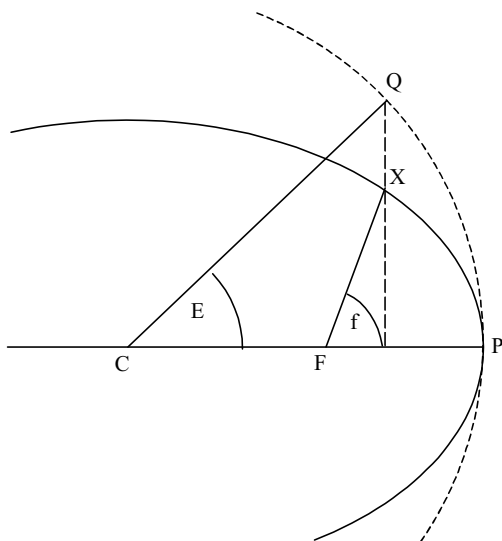

Figure 4.8: Definition of eccentric and true anomalies. The debris orbit is the solid ellipse, the debris itself at X. The centre of the ellipse is at C, its focus at F, and the perigee at P. The dashed line is part of the circumscribed circle about the ellipse that is used to define the eccentric anomaly E, which in turn is used to calculate the true anomaly of the debris, f.

$$\tan\left(\frac{f}{2}\right) = \left(\frac{1+e}{1-e}\right)^{\frac{1}{2}} \tan\left(\frac{E}{2}\right). \tag{4.7}$$

Given the true anomaly and the orbital elements, the position of the satellite can then be found in geocentric Cartesian coordinates using spherical trigonometry:

$$x = r\left[\cos\Omega\cos(\omega+f) - \sin\Omega\sin(\omega+f)\cos i\right], \tag{4.8}$$

$$y = r\left[\sin\Omega\cos(\omega+f) + \cos\Omega\sin(\omega+f)\cos i\right], \tag{4.9}$$

$$z = r\sin(\omega+f)\sin i, \tag{4.10}$$

where r = radius vector, given by:

$$r = \frac{a\,(1-e^2)}{1+e\cos f}. \tag{4.11}$$

The radius vector may also be calculated by:

$$r = a(1-e\sin E). \tag{4.12}$$

4.5 Orbital Perturbations

Up to now the equations of orbital motion above have assumed that the Earth is perfectly spherical, that its gravitational field behaves as if it were created by a point mass at its centre, that no other masses have any influence on the two-body

system, and that there are no non-gravitational forces operating in the system either.

In real life however such ideal conditions do not exist. Air drag, tidal forces from the Sun, Moon and planets, and a non-spherical gravitational field all conspire to perturb the Keplerian orbit slightly from a perfect ellipse (a fourth relativistic force also exists, but is negligible in magnitude relative to the other forces mentioned, for the case of Earth satellites).

Earth Figure

The shape of the Earth is not that of a perfect sphere. Its mass is distributed asymmetrically with the result that its gravitational potential is not homogenous. The potential can be described as that for a uniform spherical mass modified by spherical harmonic correction factors in the spherical coordinate system (r, θ, φ). The factors contain both zonal and tesseral terms, the former defining latitudinal changes in the Earth's shape with the latter defining changes with longitude. The predominant deviation from a sphere that the Earth exhibits is zonal, i.e. its equatorial bulge (Table 4.1); changes with longitude are relatively minor and affect only geosynchronous satellites. Therefore the zonal terms dominate (i.e. no φ dependence) and the expression for the gravitational potential of the Earth may be approximated to that of equation (4.13) (Aiello &Yong, 1978),

$$U \approx -\frac{GM}{r}\left[1 - \sum_{n=2}^{\infty}\left(\frac{R_e}{r}\right)^n J_n P_n(\cos\theta)\right], \qquad (4.13)$$

where r = radius, θ = latitude, R_e = Earth radius, J_n = zonal harmonic coefficients, and P_n = Legendre polynomials. The second term in the expansion is three orders of magnitude larger than higher order expansions and is the most significant; this is the term due to the equatorial bulge (Aiello &Yong, 1978). The extra mass at the equator exerts a torque on the orbit which induces gyroscopic effects, causing two major effects which can be calculated from equation (4.13).

Equatorial radius	6378.140 km
Polar radius	6356.755 km
Flattening factor f (ellipticity)	0.00335281

Table 4.1: Physical parameters of the equatorial bulge of the Earth. The difference in diameters amounts to almost 43km. In this sense the Earth is an oblate sphere. This is expanded upon in the next section.

The first effect is precession of the orbit plane, also called regression of the nodes, the rate of which can be quoted as:

$$\dot{\Omega} = -\frac{3nJ_2R_e^2}{2a^2\left(1-e^2\right)^2}\cos i,\qquad(4.14)$$

while the second effect causes a rotation of the orbit within the orbital plane, i.e. the line of apsides rotates within this plane Figure 4.9. Its rate is given by:

$$\dot{\omega} = -\frac{3nJ_2R_e^2}{2a^2\left(1-e^2\right)^2}\left(\frac{5}{2}\sin^2 i - 2\right).\qquad(4.15)$$

In both equations n is the mean motion, a, e and i are the orbital elements, and J_2 is the second zonal harmonic coefficient for the Earth, with a value of $J_2 = 0.001082$ (Weisel, 1989).
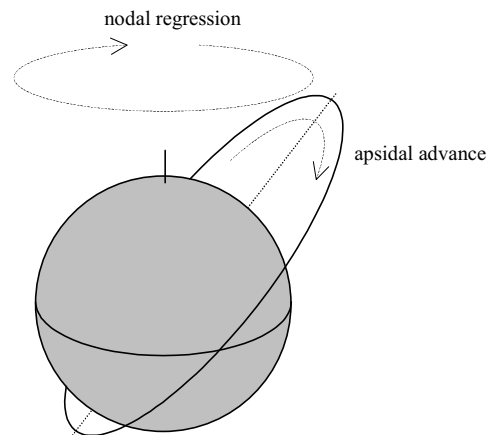

Figure 4.9: Nodal regression and apsidal advance caused by the oblateness of the Earth.

These effects are modelled in the SkyPlot program by calculating the daily movement and updating the longitiude of the ascending node and the argument of perigee between observing nights, i.e. during that jump from one night to the next which avoids daylight hours.

4.6 Position of Observer

The Earth's oblate shape means that latitude measured along the Earth's surface differs from that measured from the Earth's centre. Latitude measured with respect to the Earth's surface is termed geographic or geodetic latitude, while that measured with respect to the Earth's centre is called geocentric latitude. Conventional measurements of latitude are made using the geodetic system, so for the purposes of the SkyPlot program, which requires rectangular coordinates in a

geocentric reference frame, a conversion is necessary.

A direct conversion from a geodetic to a geocentric reference frame is explicitly given in Wertz (1978). Given a point P with a geodetic latitude ϕ and height h above the reference ellipsoid in metres, the distance d from P to the centre of the Earth (in units of the Earth's equatorial radius) is given by:
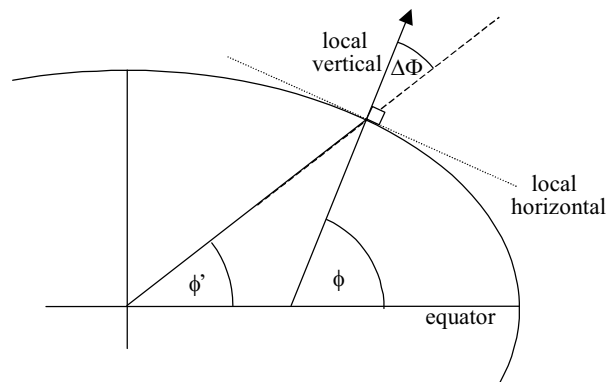

Figure 4.10: Latitude is normally expressed in terms of geodetic latitude ϕ, as measured using the local vertical which is itself perpendicular to the local horizontal, a tangent to the reference ellipsoid used to define the oblate shape of the Earth. It can be seen that geodetic latitude is not a measure of the angle between the site and the equator as measured from the Earth's centre. That distinction goes to the geocentric latitude ϕ'. The difference between the two verticals ($\Delta\Phi$) is known as the deviation of the vertical (see later). The oblateness of the Earth has been greatly exaggerated for clarity.

$$d \approx (1.5679\times10^{-7})\, h \; + \; 0.998327 \; + \; 0.001676 \cos 2\phi \; - \; 4\times10^{-6} \cos 4\phi. \quad (4.16)$$

Equation (4.16) provides the true geocentric magnitude of the radius vector of the observer. Orthogonal components used to obtain rectangular coordinates are obtained from the following expressions:

$$d \cos \phi' = (C + (1.5679\times10^{-7})\, h)\; \cos \phi, \quad (4.17)$$

$$d \sin \phi' = (S + (1.5679\times10^{-7})\, h)\; \sin \phi, \quad (4.18)$$

where

$$C \equiv \left[\cos^2\phi + (1-f)^2 \sin^2\phi\right]^{-\frac{1}{2}}, \quad (4.19)$$

and

$$S \equiv (1 - f)^2\, C \quad (4.20)$$

With these components the rectangular coordinates of the observer may be obtained. With reference to Figure 4.11,

$$x = d \cos \phi' \cos \psi, \qquad (4.21)$$

$$y = d \cos \phi' \sin \psi, \qquad (4.22)$$

and $$z = d \sin \phi' \qquad (4.23)$$

where ψ is the angle measured from the x axis towards the y axis from the abscissa, corresponding to the direction of the first point of Aries ♈.

The angle ψ_o at the beginning of each evening's observing (i.e. the resumption of observing after the daytime jump) is calculated from the time of onset of astronomical twilight. The time is converted to local sidereal time (LST), which by definition gives the position of the observing site as the angle from the vernal equinox. Thus the "start angle" of the observing site for that evening is obtained by simply converting the LST from its units of hours, to that of radians, by:
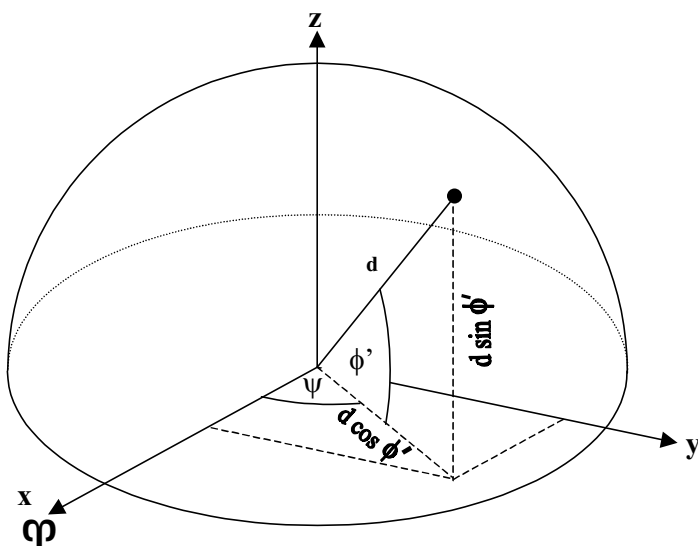

Figure 4.11: Illustration of geocentric rectangular coordinates for observer

$$\psi_o = LST_{twilight} \times 15 \times \pi / 180 \approx LST_{twilight} \times 0.261799, \qquad (4.24)$$

since one hour of sidereal time is equivalent to 15 degrees. As the length of the sidereal day is 86164.09055s, the rate at which the Earth turns on its axis (the sidereal rate, or ω_{sid}) is therefore:

$$\omega_{sid} = \frac{2\pi}{86164.09055} = 7.292116 \times 10^{-5} \; rad \; s^{-1}. \qquad (4.25)$$

Therefore at any time t, the angle ψ parallel to the celestial equator between the vernal equinox and the observer is given by:

$$\psi = \psi_o + (\omega_{sid} - t). \qquad (4.26)$$

This calculation of ψ_o is performed in the START subroutine, which is called at

the beginning of each new observing night.

4.6.1 Geocentric to geodetic alt/az correction

As a result of this oblateness the zenith produced from the radius vector of the observer (the "geocentric zenith") is different to that produced at right angles from a tangent to the Earth's surface (the "geodetic zenith"). The angle between the geocentric and geodetic zenith is called the "deviation of the vertical" (Figure 4.12), and is given by (Wertz, 1978) as

$$\Delta\Phi \approx 0.19242^{\circ} \sin 2\phi - 0.000323^{\circ} \sin 4\phi , \qquad (4.27)$$

where ϕ is the geodetic latitude. Figure 4.13 shows that the deviation of the vertical reaches a maximum value of 0.19° for a geodetic latitude of 45°.
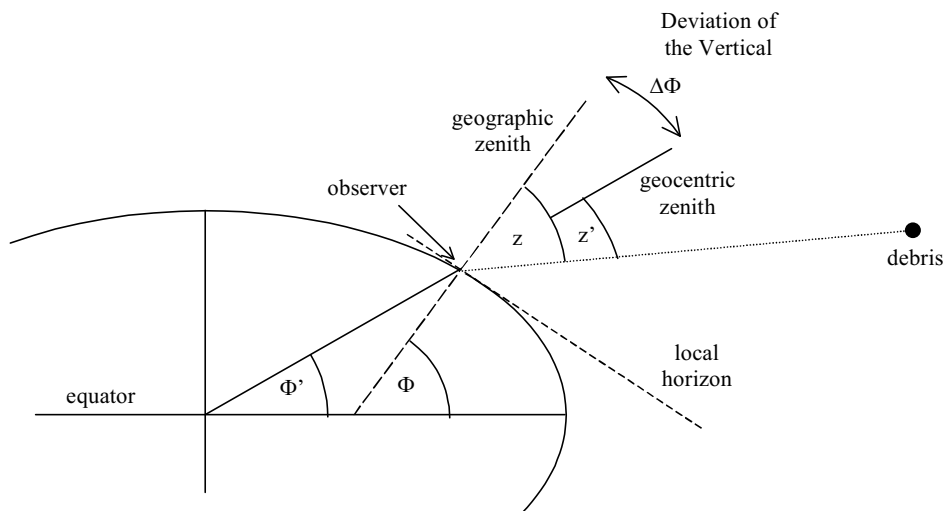

Figure 4.12: Effect of Earth oblateness on measured position of debris. For a given geographic latitude Φ the geocentric latitude Φ' can be calculated, which gives the deviation of the vertical $\Delta\Phi$. In this simplified 2D case the topocentric zenith distance of the debris (z) is given by the geocentric altitude (z') plus $\Delta\Phi$.

The initial calculation of debris altitude and azimuth uses the geocentric zenith (since the observer's radius vector is used), so a coordinate transformation is required before allocating the debris position to the correct alt/az bin. The difference in alt/az coordinates between geocentric and geodetic systems as a function of altitude and azimuth is given in Figure 4.14 which shows the difference is never more than the value at the zenith, which takes a maximum value of $\approx 0.19^{\circ}$ at 45° latitude.
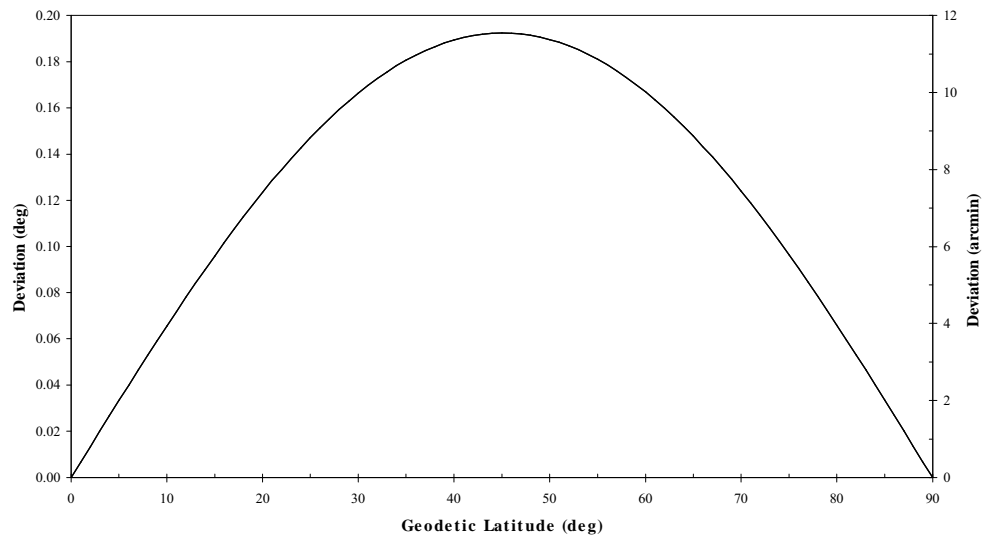
Figure 4.13: Deviation of the vertical showing maximum deviation at geodetic latitude 45º.
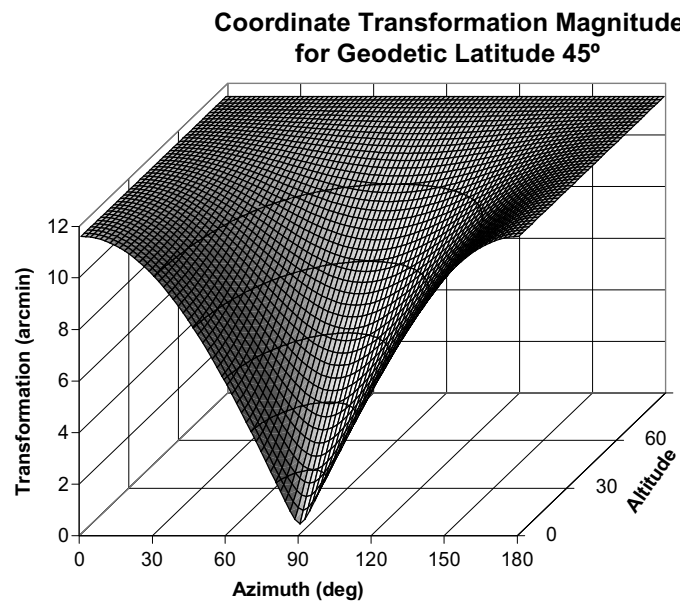

Figure 4.14: Difference between alt/az coordinates calculated in the geocentric frame and transformed to geodetic frame. The difference is nowhere greater than that at the zenith, so figures calculated for zenith only show the maximum difference. This plot is for a geodetic latitude of 45º, which has the maximum difference of about 11.4 arcmin.
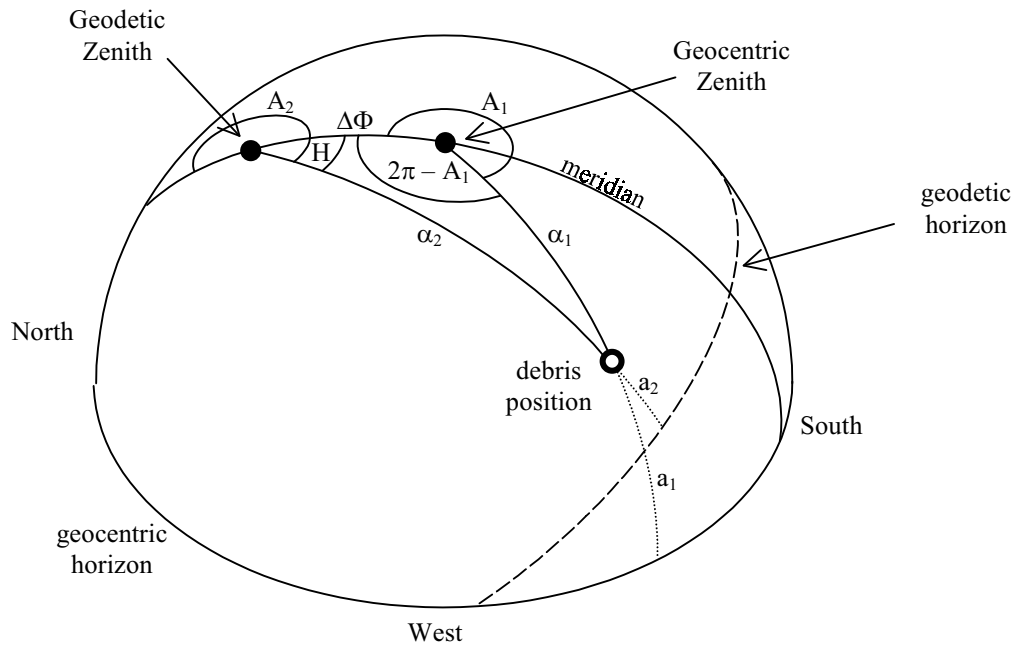
Figure 4.15: Dome of the celestial sphere about the observer, showing the transformation from geocentric to geodetic altitude/azimuth coordinates. See text for details.

With reference to Figure 4.15, the transformation from geocentric to geodetic alt/az coordinates is just the solution of a spherical triangle delineated by the geodetic and geocentric zenith, and the debris position. Given the geocentric altitude and azimuth (a_1 and A_1 respectively, the complementary geodetic altitude α_2 can be obtained from the spherical cosine equation:

$$\cos \alpha_2 \ = \ \cos \alpha_1 \cos \Delta\Phi \ + \ \sin \alpha_1 \sin \Delta\Phi \cos (2\pi{-}A_1) \, , \qquad (4.28)$$

where α_1 and α_2 are the complementary geocentric and geodetic altitudes, respectively. The complementary altitudes and the azimuth term may be rewritten to give the more convenient form of

$$\sin a_2 \ = \ \sin a_1 \cos \Delta\Phi \ + \ \cos a_1 \sin \Delta\Phi \cos A_1 \, , \qquad (4.29)$$

where a_2 is the geodetic altitude. Using the cosine formula again gives the geodetic hour angle H:

$$\cos \alpha_1 \ = \ \cos \alpha_2 \ \cos \Delta\Phi \ + \ \sin \alpha_2 \sin \Delta\Phi \cos H. \qquad (4.30)$$

So $\qquad \cos H \ = \ \dfrac{\cos \alpha_1 \ - \ \cos \alpha_2 \cos \Delta\Phi}{\sin \alpha_2 \sin \Delta\Phi} \ , \qquad (4.31)$

and $\qquad \therefore \ \cos H \ = \ \dfrac{\sin a_1 \ - \ \sin a_2 \cos \Delta\Phi}{\cos a_2 \sin \Delta\Phi} \ , \qquad (4.32)$

since α_n and a_n are complementary. As the geodetic zenith is due north (or due

south if in Southern hemisphere) of the geocentric zenith, the coordinate transformation is symmetrical about the observer's meridian i.e. an azimuth in the Eastern hemisphere will not cross the meridian into the Western hemisphere following transformation. Therefore the conversion from geodetic Hour Angle to Azimuth can be computed easily using the simple rules:

If A_1 > 180° **then** A_2 > 180° & $\therefore$ A_2 = 180° + H

If A_1 < 180° **then** A_2 < 180° & $\therefore$ A_2 = 180° − H

4.7 Earth Shadow

One of the main factors affecting satellite and debris visibility is that of eclipse; i.e. passage of the debris through the shadow cast by the Earth. As the Sun has a finite angular size the Earth's shadow consists of both an umbra and penumbra with dimensions as shown in Figure 4.16.
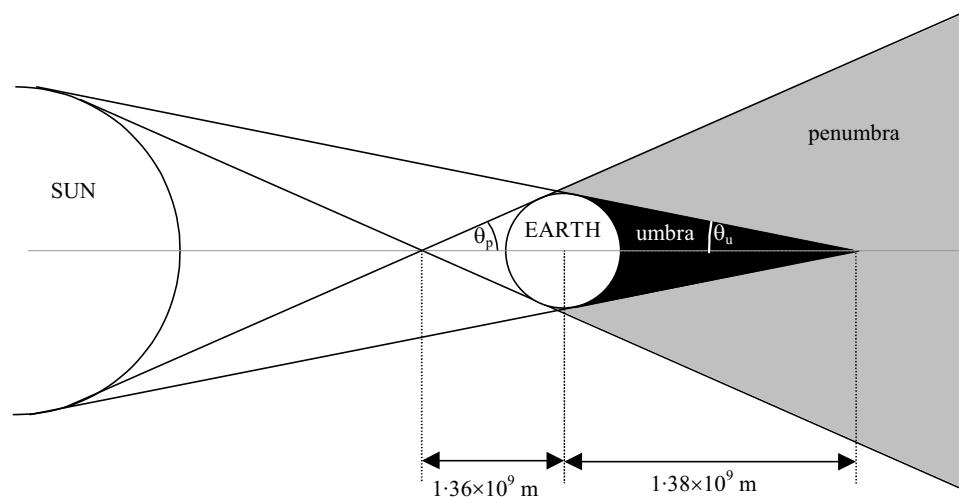

Figure 4.16: Shape of the Earth's umbra and penumbra. The half-angle of the umbra cone θ_u = 15'53" and the half angle of the penumbra cone θ_p = 16'8". Values were calculated using radii of the Sun and Earth as $6\cdot96\times10^8$ m and $6\cdot378\times10^6$ m respectively, and the distance between the two as 1 AU ($1\cdot495985\times10^{11}$ m). Note that this diagram is not to scale, causing exaggeration of the half angles, and distortion of the distances shown.

The full treatment of penumbra as well as umbra shadows when considering sunlight flux on the debris is considered in the model because duration of penumbral transit is non-negligible. Preliminary calculations showed that for circular orbits the transit duration for radial and tangential passes through the penumbra ranged from under ten seconds for a radial entry in LEO to over two minutes for a tangential entry around GSO (Figure 4.17). See Appendix 1 for

definition of radial and tangential trajectories. For elliptical orbits at apogee the velocity would be lower than that at circular velocity so the duration would be correspondingly larger. These times are of comparable size or larger than the time increment used in execution of the SkyPlot program and therefore cannot be ignored as an almost-instantaneous effect.

Vokrouhlický *et al* (1993) produced an intensive mathematical and physical model of the atmospheric refraction and absorption effects produced during penumbra transit, and showed that the main effect on solar flux attenuation was due to the apparent flattening of the solar disk as seen from the satellite (Figure 4.18) with only a minor contribution coming from the eclipsing of the solar disk by the solid Earth. They assumed the atmospheric effects to begin at a height of ~50 km.

The computations involved in the paper are lengthy and complex and their effects if incorporated into the SkyPlot program would have been to increase execution time by an unacceptable amount, hence an approximation to these effects was sought. As approximate equations to the Vokrouhlický model have yet to be developed by Vokrouhlický at time of writing, a computationally easier approximation was preferred.
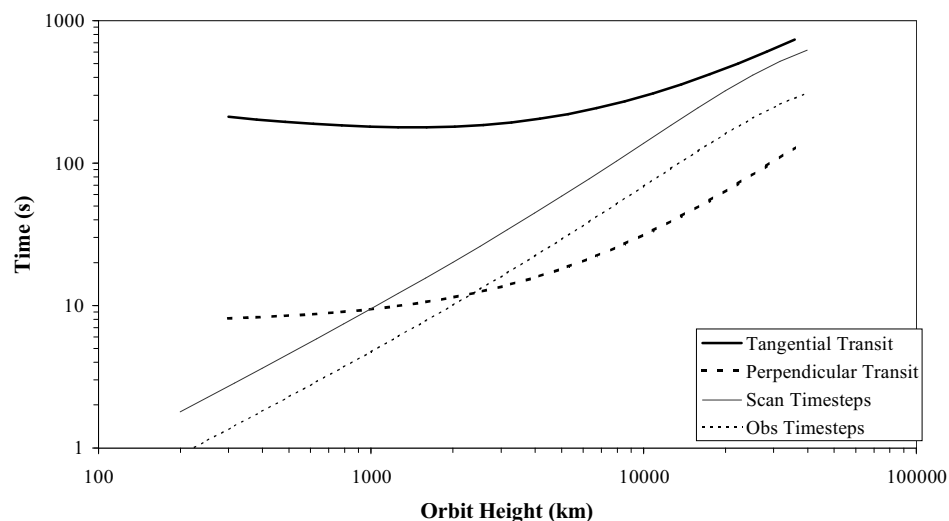

Figure 4.17: Preliminary calculations of penumbra transit duration for radial and tangential entry/exit. The calculations assumed circular orbits. Also included are curves for the scan and obs timesteps discussed earlier. See text.

As refraction effects begin when the bottom of the Sun's disk appears to touch the top of the 50 km layer of the atmosphere[*] (Figure 4.18), the flux attenuation

---

[*] Entry into the penumbra is assumed throughout this discussion.

curve is approximated by adopting an "expanded" Earth for the purposes of calculating the flux attenuation during penumbra passage only. In this case the radius of the Earth is increased by 50 km so that geometric eclipse begins at the same time that atmospheric eclipse would commence.
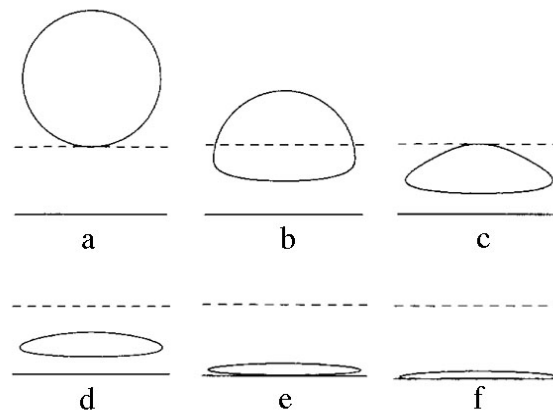

Figure 4.18: Appearance of the solar disk during passage into the penumbra. The dotted line denotes the top of the atmosphere at 50 km; the solid line is the horizon. From Vokrouhlický et al, 1993. See text for details

The apparent size of the Sun changes very little with the time of year, and when viewed from LEO to GSO, so it can be regarded as having a constant angular radius. Although the apparent size of the Earth when seen from a satellite varies with orbital altitude, if one takes the maximum altitude to be GSO then its angular radius is no smaller than $8 \cdot 7°$ or some 522'. The Earth therefore appears at least some 32 times larger than the Sun, and thus its horizon at the point of eclipse may be approximated to a straight line with only small errors induced by the lack of curvature, but with the advantage that subsequent eclipse flux calculations are much easier and therefore require less computation time. By plotting the difference between solar disk obscuration produced by an Earth disk of $8 \cdot 7°$ radius, and that of a flat horizon, Figure 4.19 shows that the maximum possible increased obscuration effect produced by the flat horizon does not exceed 0.35% of the solar disk.

The paper by Vokrouhlický was concerned with solar radiation pressure on satellites during penumbral transit, and contained graphs of the transverse (i.e. parallel to velocity vector) acceleration component on existing and theoretical satellites. As these satellites were modelled to be spherically symmetric (i.e. no variation of acceleration was produced by attitude variation of the spacecraft), and as

the geocentric arclength of the orbit through the penumbra was typically ~1%

**Overestimation of Solar Disk Obscuration
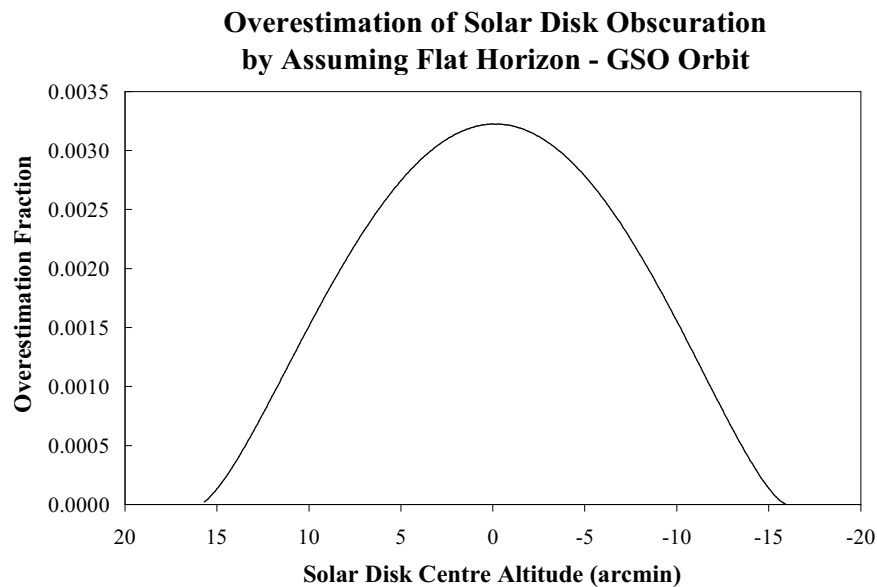by Assuming Flat Horizon - GSO Orbit**

Figure 4.19: Error induced by approximating the obscuring Earth horizon as a straight line, for the worst-case scenario of maximum apparent Earth curvature at GSO.

of orbital period, which for a circular orbit implies an arclength of 3.6º, so that the angle between the solar radiation pressure force and velocity vector also changed by 3.6º, then one can assume that practically all of the variation in transverse acceleration in the graphs was produced by the variation in solar flux. Therefore normalising the ordinate produces graphs of normalised solar flux values.

This provided "realistic" examples of penumbra immersion against which to test the expanded-Earth non-atmospheric flat-horizon model. The LEO example in the paper by Vokrouhlický consisted of a simulated LAGEOS[*] penumbra entry such that the trajectory of the setting solar disk was at 43º to the normal to the local horizon as viewed from LAGEOS. The abscissa was given as time after first contact with the top of the 50 km atmosphere layer; this was converted to arcminutes of the geometric (unrefracted) centre of the Sun's disk above the horizon to remove dependency on geometry and orbital period in comparison calculations. The results of the comparison are shown in Figure 4.20.

It can be seen that the expanded-Earth model underpredicts the solar flux at LAGEOS (and hence its brightness) by as much as 40%. The long tail of the Vokrouhlický model is described in the paper as being due almost entirely to refraction effects; actual eclipsing of the flattened solar disk not beginning until

---

[*] A passive, laser-tracked satellite in a 5900km circular polar orbit.
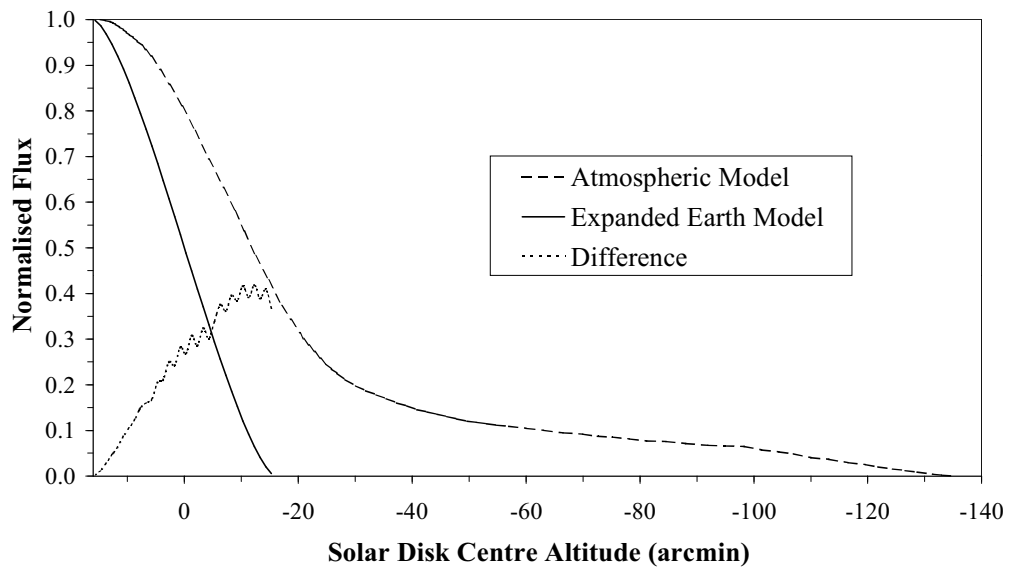
the very end (near the –100' mark).

Figure 4.20: LEO comparison of penumbra illumination models. The jagged appearance of the difference curve is due entirely to sampling noise between the two other curves' nonaligned data points. See text for discussion.

The graph for GSO orbit shows that the difference between the two models is much smaller (Figure 4.21). This is due to the fact that the observed thickness of the 50 km-width atmosphere constitutes a much smaller fraction of the unflattened observed solar diameter at higher altitudes (12.8% instead of 315% at 250 km), i.e. there is less difference between this case and an airless Earth. The general trend by adopting this method is therefore that the brightness of debris in the penumbra is underpredicted at all times, by an amount inversely proportional to orbit height. At LEO the underprediction peaks at 40% while in GSO the difference does not rise above 10%. The poor LEO prediction is not as important however, as the debris only stays in the penumbra for a short time. In the absence of any simple and quick-to-execute method of approximating the penumbra brightness of debris, the airless expanded Earth model will have to suffice for now.
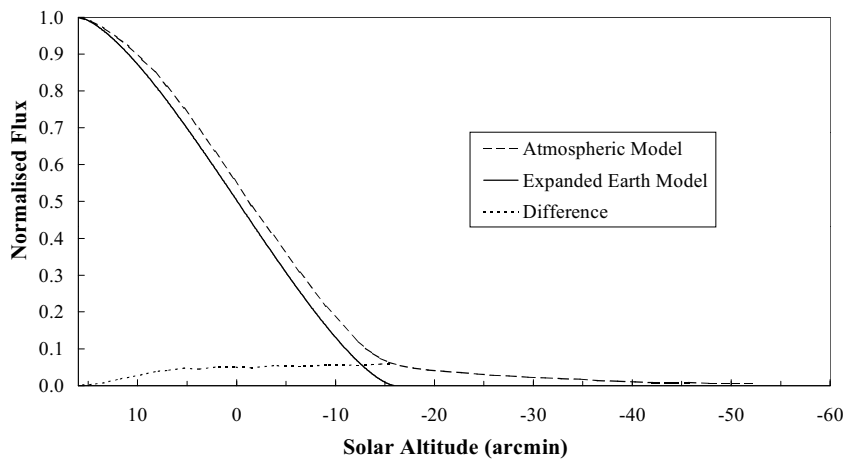
Figure 4.21: As for previous figure but for simulated satellite in geostationary orbit.

Coding: Shadow entry criteria

The SkyPlot program treats the Earth's umbra and penumbra with a structure as in Figure 4.16. The situation is rotationally symmetric about the shadow cone axis and thus the problem reduces to a two-dimensional case involving just the plane containing the shadow cone axis and the debris position vector.

The geometry for calculation of umbral and penumbral eclipse events is shown schematically in Figure 4.22.
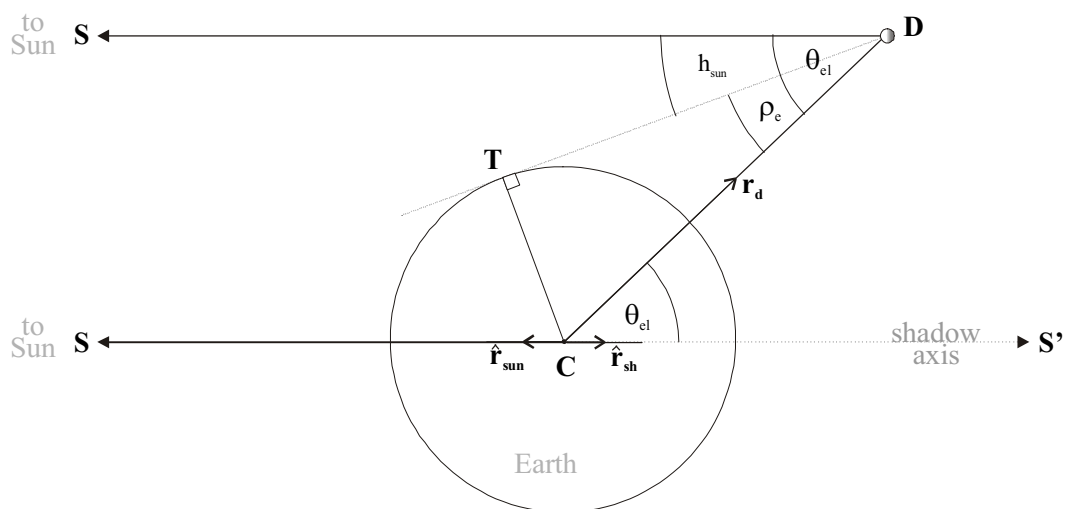

Figure 4.22: Geometry for determination of eclipse events. See text for details.

With reference to Figure 4.22, the centre of the Earth is shown at C, the debris at D, and the Sun is taken to be off the left of the page at S. The unit vector of the Sun's direction is shown as $\hat{r}_{sun}$, while that of the Earth's shadow axis $\hat{r}_{sh}$ is by definition in the opposite direction, i.e.:

$$\hat{\mathbf{r}}_{sh} = -\hat{\mathbf{r}}_{sun} \ . \tag{4.33}$$

The apparent separation angle θ_{el} between the centres of the Earth and the Sun, from the viewpoint of the debris, is calculated from the scalar product of the debris vector $\mathbf{r_d}$ and the shadow axis vector $\hat{\mathbf{r}}_{sh}$ (since CS' is parallel to SD), as:

$$\cos\theta_{el} = \frac{\hat{\mathbf{r}}_{sh} \cdot \mathbf{r_d}}{|\hat{\mathbf{r}}_{sh}||\mathbf{r_d}|} = \frac{\hat{\mathbf{r}}_{sh} \cdot \mathbf{r_d}}{|\mathbf{r_d}|} \ . \tag{4.34}$$

Projecting a tangent to the Earth's surface at T from the debris at D enables us to calculate the apparent angular radius of the Earth ρ_e from the same viewpoint of the debris, as:

$$\sin\rho_e = \frac{CT}{CD} = \frac{r_e^{'}}{|\mathbf{r_d}|} \ . \tag{4.35}$$

The apparent angular radius of the Sun ρ_s is taken to be a constant with a value of $\rho_s = 4.66003\times10^{-3}$ radians (Allen, 1973).

The apparent altitude of the of the centre of the Sun's disk h_{sun} is therefore defined by:

$$h_{sun} = \theta_{el} - \rho_e \ . \tag{4.36}$$

The scenario of full illumination of the debris, depicted by Figure 4.22, observed from the viewpoint of the debris is shown in Figure 4.23(a). During the penumbral phase of shadow entry/exit, when the Sun's disk is partially obscured by the Earth's limb, the view is shown in Figure 4.23(b).
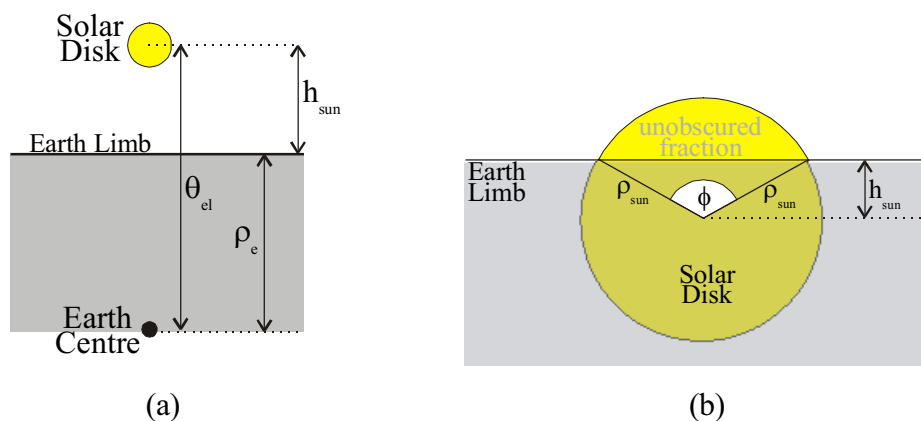

(a)   (b)

Figure 4.23: (a) Debris-eye view of Figure 4.22, not to scale. Note that θ_{el}, ρ_e and h_{sun} are arcs, not linear dimensions. (b) Debris-eye view of the Sun during Earth penumbral transit, showing construction for determination of the part of the Sun's disk unobscured by the Earth's limb. See text for details.

The relationship between h_{sun} and the sector angle ϕ is given by

$$\phi = 2\cos^{-1}\left[\frac{-h_{sun}}{\rho_{sun}}\right] , \tag{4.37}$$

where the negative of h_{sun} is used to obtain ϕ in the correct range. The normalised area of the exposed part of the solar disk is therefore given by:

$$A_{sun} = \frac{\frac{1}{2}\rho_{sun}^2\left[\phi - \sin\phi\right]}{\pi\rho_{sun}^2} \tag{4.38}$$

$$= \frac{\phi - \sin\phi}{2\pi} \tag{4.39}$$

The solar flux on the debris is therefore taken to be just the Solar constant for the wavelength and bandwidth used, multiplied by the factor A_{sun}. Sample curves showing the fall-off of illumination for a radial entry into the penumbra are given in Figure 4.24.

The SkyPlot program therefore identifies three cases of debris illumination:

Case 1: Debris fully illuminated   for $\rho_{sun} < h_{sun} \le \pi$

Case 2: Debris partially illuminated   for $-\rho_{sun} < h_{sun} < \rho_{sun}$
         (in Earth's penumbra)

Case 3: Debris not illuminated   for $-\pi \le h_{sun} < -\rho_{sun}$
         (in Earth's umbra)

SkyPlot calculates SNR for cases 1 & 2 if the debris is above the observer's horizon at night, but not for case 3.
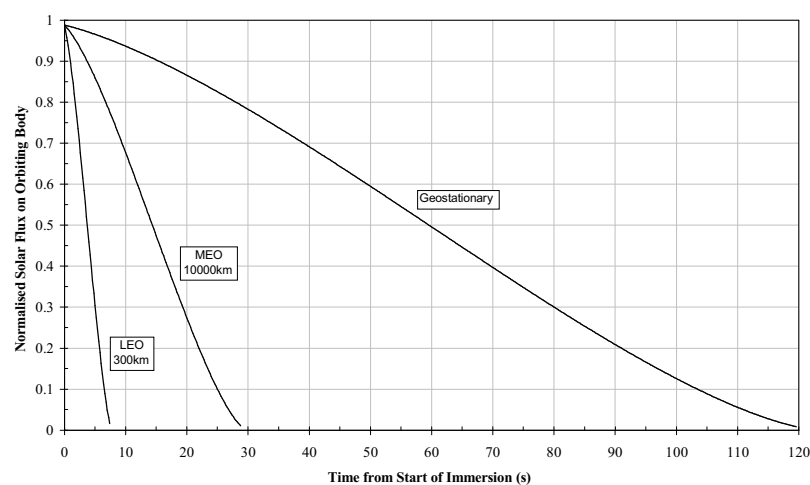

Figure 4.24: Sample penumbra flux curves using flat Earth model with no atmosphere and radius increased by 50km.

4.8 Topocentric Angular Velocity

Both debris and observer are moving about the centre of the Earth, their motions described by position and velocity vectors. The apparent angular velocity of the debris from the point of view of the observer (the "topocentric angular velocity", or ω_{top}) is calculated from the relative position and velocity vectors, which are calculated separately below.

Analytical investigations into the maximum angular speed of debris to be expected under various special cases of observing site latitude/zenith distance and orbital height/inclination/eccentricity were performed in chapter 2. This section describes how the angular speed is calculated generally for the purposes of the SkyPlot program.

4.8.1 Observer velocity

The path of the observer describes a circle about the polar axis of the Earth, its plane parallel to the equator. The radius of the circle is proportional to the cosine of the latitude ϕ of the observer, plus the observer's height above sea level. In section 4.6 the rectangular components of the observer position were given in units of the Earth's equatorial radius R_e, taking into account the oblateness of the Earth's shape. The true geocentric distance r_g from the Earth's centre to the observer is reproduced here coupled with the geocentric latitude ϕ' (the geodetic latitude is shown as ϕ):

$$r_g \cos \phi' = (C + (1.5679 \times 10^{-7}) h) \cos \phi , \qquad (4.40)$$

where

$$C \equiv \left[\cos^2 \phi + (1 - f)^2 \sin^2 \phi \right]^{-\frac{1}{2}} \qquad (4.41)$$

and

$$S \equiv (1 - f)^2 C \qquad (4.42)$$

and where f is the flattening factor or ellipticity of the Earth's form, with a value of $f = 0.00335281$. Thus it can be seen that the radius of the circle of observer's motion is given by equation (4.40). The angular velocity about the axis is just the sidereal rate of $\omega_{sid} = 7.292116 \times 10^{-5}$ radians s^{-1}.

The relation between linear velocity v, radius r and angular velocity ω, $v = r \omega$,

applied here, gives the linear velocity of the observer:

$$v_{obs} = r_g \cos \phi' \cdot \omega_{sid} . \tag{4.43}$$

The observer's velocity vector is always perpendicular to its position vector (for circular motion). The Cartesian components of the position vector are (from section 4.6):

$$x = r_g \cos \phi' \cos \psi \tag{4.44}$$

and

$$y = r_g \cos \phi' \sin \psi , \tag{4.45}$$

where

$$\psi = \psi_o + (\omega_{sid} \cdot t) . \tag{4.46}$$

Therefore the Cartesian components of the observer's velocity vector $\mathbf{v_o}$ are

$$\dot{x}_o = r_g \cos \phi' \sin \psi , \tag{4.47}$$

$$\dot{y}_o = r_g \cos \phi' \cos \psi , \tag{4.48}$$

and

$$\dot{z}_o = 0 . \tag{4.49}$$

There is no z component as there is no motion parallel to the Earth's axis.

4.8.2 Geocentric debris velocity

Cartesian components of an orbiting body's geocentric velocity are given in Roy (1988, p103). The components of the debris velocity vector $\mathbf{v_d}$ are:

$$\dot{x}_d = \frac{n\,a}{r} \cdot (b\, l_2 \cos E - a\, l_1 \sin E) , \tag{4.50}$$

$$\dot{y}_d = \frac{n\,a}{r} \cdot (b\, m_2 \cos E - a\, m_1 \sin E) , \tag{4.51}$$

and

$$\dot{z}_d = \frac{n\,a}{r} \cdot (b\, n_2 \cos E - a\, n_1 \sin E) , \tag{4.52}$$

where n, a, r, b and E, as defined earlier in this chapter, are the mean motion, semimajor axis, radius vector, semiminor axis and eccentric anomaly respectively, while l,m,n are the direction cosines of two orthogonal geocentric axes in the orbit plane and aligned with the semimajor (subscript 1) and semiminor (subscript 2) axes, such that:

$$l_1 = \cos \Omega \cos \omega - \sin \Omega \sin \omega \cos i , \tag{4.53}$$

$$m_1 = \sin \Omega \cos \omega + \cos \Omega \sin \omega \cos i , \tag{4.54}$$

$$n_1 = \sin \omega \sin i , \tag{4.55}$$

and

4-27

$$l_2 = -\cos \Omega \sin \omega \ - \ \sin \Omega \cos \omega \cos i \ , \tag{4.56}$$

$$m_2 = -\sin \Omega \sin \omega \ + \ \cos \Omega \cos \omega \cos i \ , \tag{4.57}$$

$$n_2 = \cos \omega \sin i \ , \tag{4.58}$$

where Ω, ω and i are orbital elements defined earlier in the chapter as the longitude of the ascending node, argument of perigee, and orbital inclination, respectively.

4.8.3 Topocentric angular velocity

The linear velocity of the debris with respect to the observer is obtained from the relative vector $\mathbf{v_{do}}$, such that:

$$\begin{aligned} v_{do} &= v_d - v_o \\ &= \left[\left(\dot{x}_d - \dot{x}_o \right), \left(\dot{y}_d - \dot{y}_o \right), - \dot{z}_d \right] \end{aligned} \tag{4.59}$$

To find the instantaneous topocentric angular velocity, the magnitude of the component of $\mathbf{v_{do}}$ perpendicular to the line of sight, $|\mathbf{v_{do}}|_\perp$ must be obtained. This is achieved by first calculating the angle between the relative position vector $\mathbf{r_{do}}$ and the relative velocity vector $\mathbf{v_{do}}$ (using the scalar product), then multiplying $|\mathbf{v_{do}}|$ by the sine of that angle (which applies for both acute and obtuse angles) - see Figure 4.25.
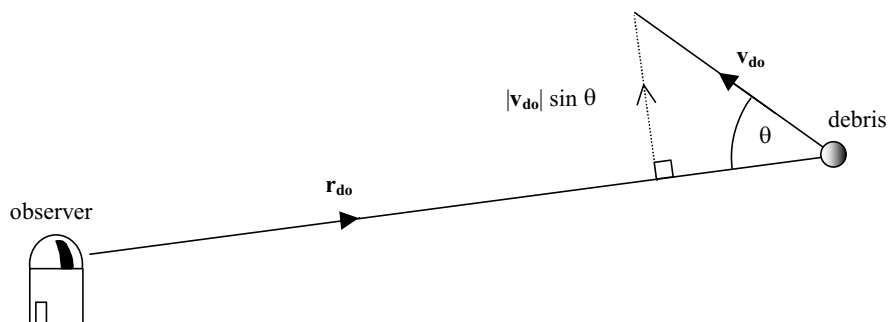

Figure 4.25: Calculation of ω_{top} from relative vectors of position and velocity.

Thus

$$\cos \theta \ = \ \frac{r_{do} \cdot v_{do}}{|r_{do}| \ |v_{do}|} , \tag{4.60}$$

the perpendicular component is:

$$|\mathbf{v_{do}}|_\perp \ = \ |\mathbf{v_{do}}| \sin \theta \ , \tag{4.61}$$

and the topocentric angular velocity is given by:

$$\omega_{top} = \frac{|v_{do}|_{\perp}}{|r_{do}|} \text{ (radians s}^{-1}) .$$
(4.62)

4.8.4 Topocentric Angular Velocity Binning

The angular velocity ceiling was set to 100 arcmin s^{-1}, stepped in increments of 5 arcmin s^{-1}, giving twenty bins. The equation in the binning algorithm of SkyPlot is:

$$\texttt{Bin\#=int[(ω_{top}*RD*60)/5]+1} ,$$
(4.63)

where RD = radians to degrees factor = $180 / \pi$.

4.9 Solar Motion

The motion of the Sun cannot be ignored throughout execution of the program; its position determines the onset of sunset/sunrise twilight and the position of the Earth's penumbral and umbral shadow cones. The calculation of the Sun's position is straightforward but lengthy (Duffett-Smith, 1988); to perform this calculation for every time increment would consume computing power unnecessarily. The Sun moves across the celestial sphere at an average rate of 0.986º/day. Considering the fact that the alt-az resolution of the bins in the program output is nominally 2º, the Sun's position need only be updated once every two days as the mean effect on the umbra is acceptable.

4.10 The Moon

This section discusses the effect moonlight has on debris observations, and of calculating its position during the observing run.

4.10.1 Sky Brightness due to Moonlight

The additional brightness of the night sky due to scattered light from the Moon when it is above the observer's horizon is modelled using equations by Schaefer (1993), and reproduced here.

The linear brightness value of the sky in nanoLamberts (nL), caused solely by scattered moonlight, B_{moon}, is given by:

$$B_{moon} = f(\rho_{moon}) \; 10^{\{-0.4[m_{moon}+16.57+kX(Z_{moon})]\}} \; \{1-10^{[-0.4kX(Z)]}\} \; nL \; , \qquad (4.64)$$

where m_{moon} = magnitude of the Moon, k = atmospheric extinction factor in magnitudes per airmass, $X(Z)$ = airmass as a function of zenith distance of Moon (using Z_{moon}), and look angle (using Z), and $f(\rho_{moon})$ = scattering function as function of the separation angle ρ_{moon} between the look angle and the Moon. Each of these terms is now described in more detail.

The magnitude of the Moon for a given phase angle α in degrees is given by:

$$m_{moon}(\alpha) = -12.73 + 0.026|\alpha| + 4\times10^{-9}\alpha^4 \; , \qquad (4.65)$$

where $\alpha = 0°$ for a full Moon.

The airmass function for the observer's look angle is given by:

$$X(Z) = \sec Z = \frac{1}{\sin(\text{altitude})} \; , \qquad (4.66)$$

which is adequate for this purpose as observations do not range below 10° altitude.

The airmass function applied to the Moon's zenith distance Z_{moon} is given by:

$$X(Z_{moon}) = \frac{1}{\sqrt{(1-0.96 \; \sin^2 Z_{moon})}} \; . \qquad (4.67)$$

This function is different to that used for the look angle as it gives a better fit to observed scattered moonlight data (Krisciunas and Schaefer, 1991).

The scattering function $f(\rho_{moon})$ is given by:

$$f(\rho_{moon}) = 10^{5.36} \left[1.06+\cos^2 \rho\right] + 10^{[6.15-(\rho/40°)]} + 6.2\times10^7\rho^{-2} \; . \qquad (4.68)$$

4.10.2 Lunar Motion

Like the Sun, the Moon's position is updated at a frequency related to its average angular velocity and the size of the alt-az (sky) bin for the output array. In the case of the Moon, the mean sidereal motion of 13.176358° per day is adopted (Allen, 1973), leading to an average motion of :

$$\frac{13.176358°}{T_{SD}} \times 3600 = 0.5505° \text{ per hour} , \qquad (4.69)$$

where T_{SD} = sidereal day = 86164.09s. Thus with 2° sky bins, the Moon's position need only be updated every 3.6329 hours, or approximately 13,000 seconds.

Given an accurate position of the Moon for the start of the night's observing, subsequent positions may be calculated for the rest of the night by extrapolating from the first position calculated for that night using the Moon's hourly motion, rather than repeat the lengthy calculation every three hours throughout the night. The error induced by this is sufficiently small for this to be a viable method of calculation, thus shortening execution time.

Figure 4.26 below shows the error drift throughout the night for a sample date between the lunar positions calculated fresh each time and those calculated using the hourly motions derived from the first position. It can be seen that the final error for that date is well within the size of the 2º sky bins. Figure 4.27 depicts the error after 12h for each day throughout a typical year, showing that although there is a large variation, the maxima are less than 0.4º. Thus this technique is a viable method of calculating the Moon's position faster, with acceptable error. Calculations used here and in SkyPlot were based on routines in Duffett-Smith, (1987).
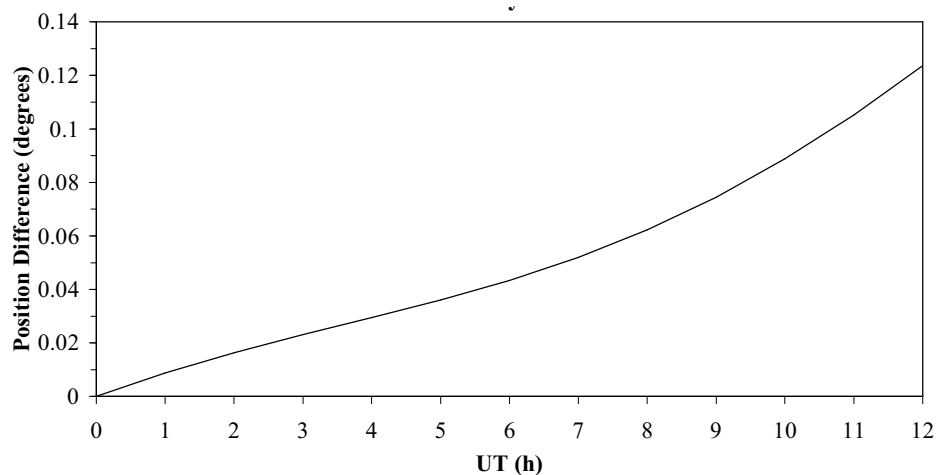

Figure 4.26: The difference between performing a complete calculation of the Moon's position every hour, and using the Moon's hourly motion deduced from its first position result. Over this 12 hour period the difference amounts to less than one-fifth of a degree by the end of the period.
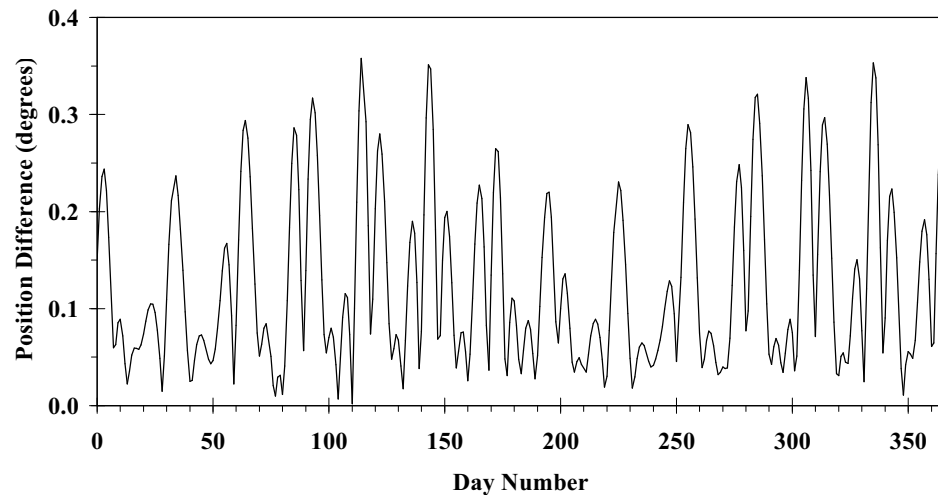
Figure 4.27: The end-of-12h-period figures for each day of 1990. Although there is a large variation in difference, the maxima are not larger than 0.4º, much smaller than the size of skybin (see text).

The algorithm with regard to this method of calculation is as follows:

1. Calculate first position of Moon at beginning of night using complete routine to obtain initial right ascension and declination values (α_0, δ_0).

2. Determine hourly motions in right ascension $\Delta\alpha$ and declination $\Delta\delta$ using data from this first calculated position.

3. Use $\alpha_t = \alpha_0 + \Delta\alpha$ and $\delta_t = \delta_0 + \Delta\delta$ to obtain subsequent coordinates of Moon for all other times throughout the night.

4.11 Milky Way

From the Earth's viewpoint, our home galaxy is visible to the naked eye as a broad irregular band of light crossing the celestial sphere in a great circle, the average number of stars per unit area decreasing with galactic latitude.

The Milky Way's contribution to the background sky brightness is obtained from a table of integrated star light (Allen, 1973, p245) as a function of galactic latitude, given in units of the equivalent number of 10th magnitude stars per square degree, or "S10" units, which are converted to SI units in section 4.14.
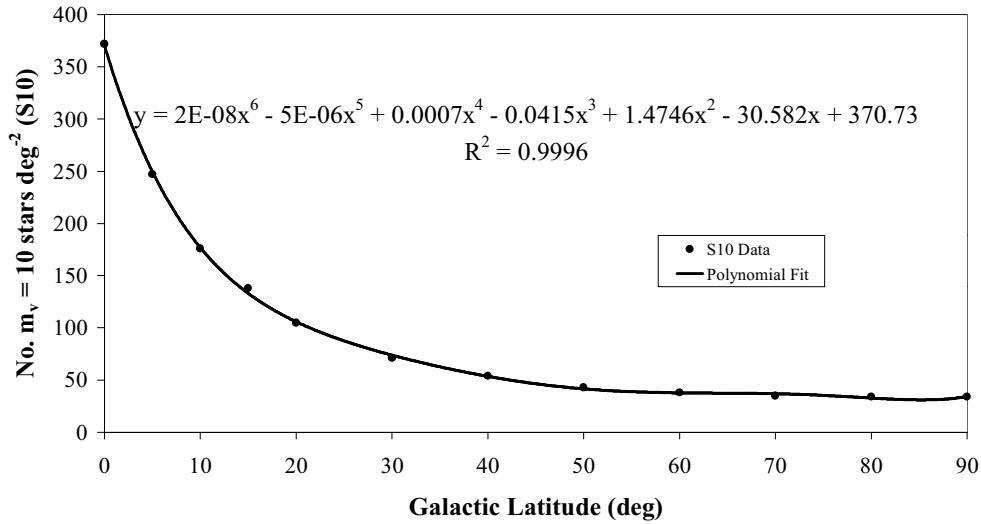
Figure 4.28: Brightness density of the Milky Way as a function of galactic latitude. The units of brightness are given as the equivalent number of 10th magnitude stars per square degree (S10). Details of the sixth-order polynomial fit to the data are shown.

Values of galactic background for intermediate latitudes are calculated by using a sixth-order polynomial fit to the data (Figure 4.28). To facilitate program execution speed, these values are calculated to the nearest degree of latitude and stored in a lookup array before the time-intensive part of the program begins. This model therefore does not feature any inhomogeneity with galactic longitude.

Galactic latitude is calculated using the Horizon-Galactic coordinate transformation matrix (Duffett-Smith, 1988) which requires the Cartesian coordinates of the observer-debris look angle. This is used rather than the standard equation to transform equatorial coordinates to ecliptic because an additional calculation would have to be made to derive the equatorial coordinates from the initial Cartesian values. The matrix method obviates this first step. As only galactic latitude is required, only the bottom row of the transformation matrix is used, so that the final calculation for galactic latitude reduces to:

$$b = \sin^{-1}\left[\frac{(x_{do} \cdot g + y_{do} \cdot h + z_{do} \cdot i)}{s_{do}}\right] , \qquad (4.70)$$

where x_{do}, y_{do}, and z_{do} are the Cartesian components of the debris-observer position vector, s_{do} is the magnitude of the position vector (present to convert the components to unit vectors), and the terms g, h, and i are the conversion matrix components i = -0.8676008, j = -0.1883746, and k = 0.4601998 respectively.

4.12 Zodiacal Light

Like the Milky Way, the Zodiacal Light is a source of background noise that can degrade the SNR of a debris detection. It is symmetrical about the ecliptic plane and about the solar longitude. It peaks at the position of the Sun, and drops with ecliptic latitude and elongation from the Sun, though a small peak is observable at the anti-sun position, called the Gegenschein (Figure 4.29). Data for the ecliptic variation of zodiacal light brightness have been determined (Levasseur-Regourd & Dumont, 1980), and were included in this study as a lookup table, which was accessed by calculating the ecliptic coordinates from the Cartesian debris-observer relative vector components, using the transformation matrix featured in Duffet-Smith (1988, p50):

$$
\begin{pmatrix} m \\ n \\ p \end{pmatrix}_{\lambda,\beta} = \begin{pmatrix} 1 & 0 & 0 \\ 0 & \cos\varepsilon & \sin\varepsilon \\ 0 & -\sin\varepsilon & \cos\varepsilon \end{pmatrix} \cdot \begin{pmatrix} x \\ y \\ z \end{pmatrix}_{\alpha,\delta} \tag{4.71}
$$

Here ε = mean obliquity of the ecliptic. The epoch 2000.0 value of $\varepsilon = 23.43°$ was treated as a constant because great accuracy was not required due to the size of the zodiacal array cells.

4.13 Refraction

The Earth's atmosphere refracts light such that the zenith distance of an object appears smaller than it would be if there were no refraction. Thus if z is the true zenith distance, z' the observed zenith distance after refraction, and R is the change in zenith distance due to refraction, then z' = z – R.
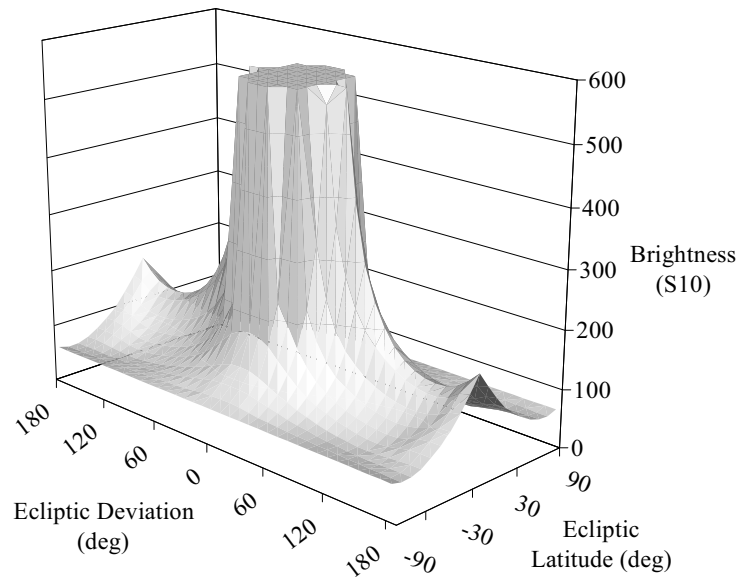
Figure 4.29: Variation of the zodiacal light with ecliptic latitude and the ecliptic longitude separation to the Sun. The brightness is symmetric about the longitude of the Sun, and the ecliptic. The brightening 180º from the Sun is due to the Gegenschein. Units of brightness are in number of 10th magnitude stars per square degree (see text).

The magnitude of R is a function of zenith distance and the prevailing meteorological conditions at the observing site. A rough expression for R is usually expressed as (Duffett-Smith, 1988):

$$R = \frac{0.00452° \, P \tan z}{(273 + T)} \text{ (degrees)},$$
(4.72)

where P = barometric pressure (mb) and T = atmospheric temperature (K). This expression is accurate to ~ 6" in the zenith distance range of 0º-75º. Although observations of faint objects are rarely if ever undertaken at zenith distances above 60º due to atmospheric extinction, for completeness' sake the more appropriate approximate formula for zenith distances in the 75º-90º range is given below (Duffett-Smith 1988):

$$R = \frac{P\left(0.1594 + 0.0196a + 2 \times 10^{-5}a^2\right)}{(273 + T)\left(1 + 0.505a + 0.0845a^2\right)}.$$
(4.73)

The maximum value of R is 0.5º at STP at sea level for objects on the horizon, and correspondingly less nearer to the zenith.

**Atmospheric Refraction
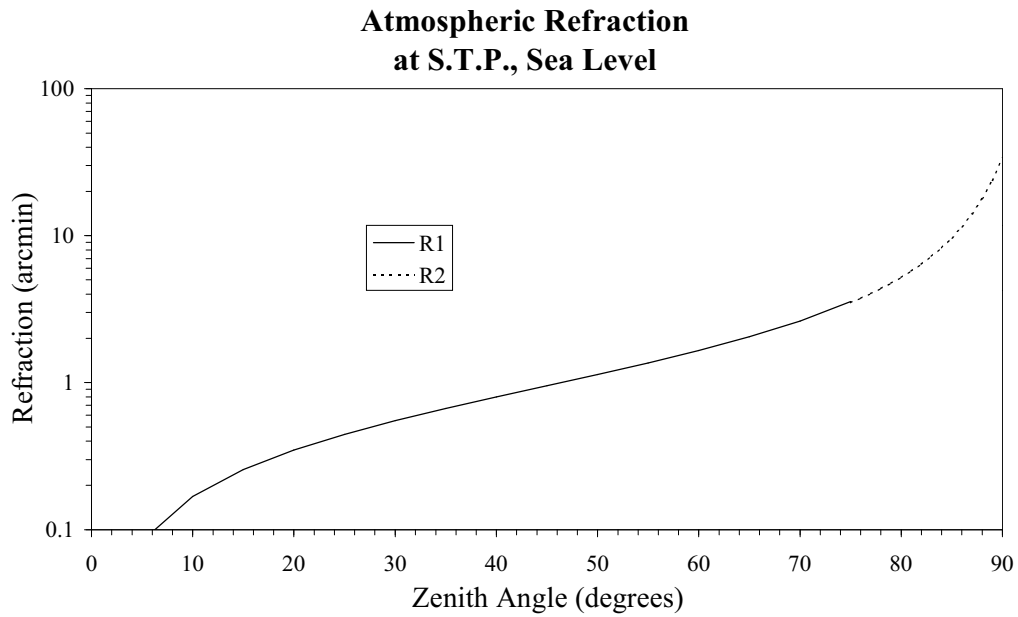at S.T.P., Sea Level**

Figure 4.30 Angular difference in zenith distance due to atmospheric refraction. "R1" refers to the expression used for the zenith distance range 0-75º, while "R2" refers to that for the range 75-90º.

Given that the size of skybin is 2°×2° in SkyPlot, the effects of refraction are relatively minor.

4.14 Debris Signal-to-Noise Ratio (SNR)

The SNR calculation is performed once most of the decision-making criteria are met to deem the debris as "visible", i.e. the debris is above the observer's horizon and out of the Earth's shadow cone, while the Moon is below the horizon and the Sun is at least 18º below the horizon, ensuring the sky is astronomically dark.

The SNR equation is calculated as:

$$SNR = \frac{S_{deb}}{\left[\left(S_{deb} + S_{sky} + S_{moon} + S_{gal} + S_{zod}\right)^{\frac{1}{2}} + S_{readout}\right]},$$
(4.74)

where S_{deb} = signal from the debris, S_{sky} = signal from the night sky, S_{moon} = signal from scattered moonlight, S_{gal} = integrated signal from stars in the Milky Way, S_{zod} = signal from the Zodiacal Light, and $S_{readout}$ = readout noise inherent in the CCD. The individual signals are now discussed.

4.14.1 Debris Flux Calculation

4.14.1.1 Debris Brightness

Consider light incident from the Sun on a spherical debris particle of radius r_{deb}. The power (per nanometer wavelength) intercepted by the debris, P_{int}, is given by:

$$P_{int} = sol_{600}\, \pi r_{deb}^2 \qquad (W\ nm^{-1})\,, \qquad (4.75)$$

where $sol_{600} = 1.752\ W\ m^{-2}\ nm^{-1}$, the solar constant at the top of the Earth's atmosphere, at a central wavelength of 600nm.

Treating the debris particle initially as a flat lambert disc of the same radius, the incident light is reflected into π steradians (Figure 4.31).
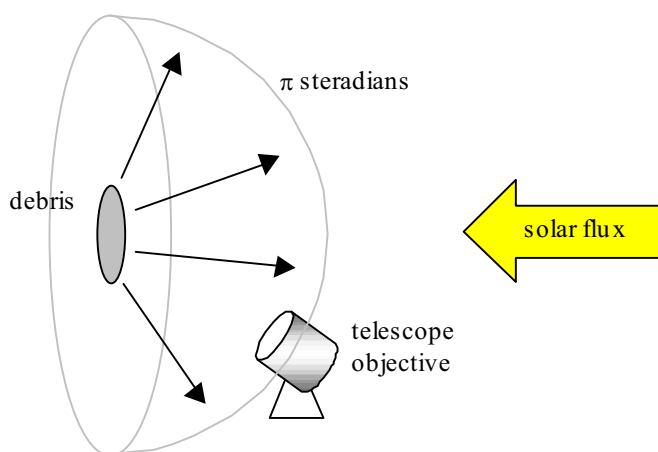

Figure 4.31: Reflection off lambert sphere treated as disk.

Reflected intensity must be modified by the Bond Albedo A_b for a lambert sphere, given in section 1.3.3, and reproduced here for clarity:

$$A_b(\phi) = 0.3299 \frac{2}{3\pi}\left[\sin\phi + (\pi - \phi)\cos\phi\right], \qquad (4.76)$$

where ϕ = phase angle (light source – debris – observer). The reflected intensity I_{deb} from the debris is therefore given by:

$$I_{deb} = \frac{sol_{600}\, \pi r_{deb}^2\, A_b(\phi)}{\pi} \qquad (W\ nm^{-1}\ sr^{-1}). \qquad (4.77)$$

Now, the solid angle Ω_{tel} subtended by the telescope objective of radius r_{tel}, at the debris-observer distance d, is given by:

$$\Omega_{tel} = \frac{\pi r_{tel}^2}{d^2} \qquad (sr)\,, \qquad (4.78)$$

so that this solid angle intercepts light reflected from the debris particle.

The effect of atmospheric extinction must also be taken into account, however. The Earth's atmosphere both absorbs and scatters light, causing a reduction in brightness of the source, an effect termed "extinction". This attenuation factor "Ext" must be multiplied by the power from the debris, and is given below (Schaefer, 1993):

$$\text{Ext} = 10^{\left\{ \frac{-\left(k/2.5 \right)}{\sin(\text{alt})} \right\}}, \tag{4.79}$$

where k = extinction coefficient (magnitudes per airmass), and alt = altitude of the debris (above observer's horizon). The value of k varies from site to site and with time of year, but is usually of the order of 0.10–0.15 for astronomical sites (Schaefer, 1993). The behaviour of Ext for different examples of observing site is shown in Figure 4.32.
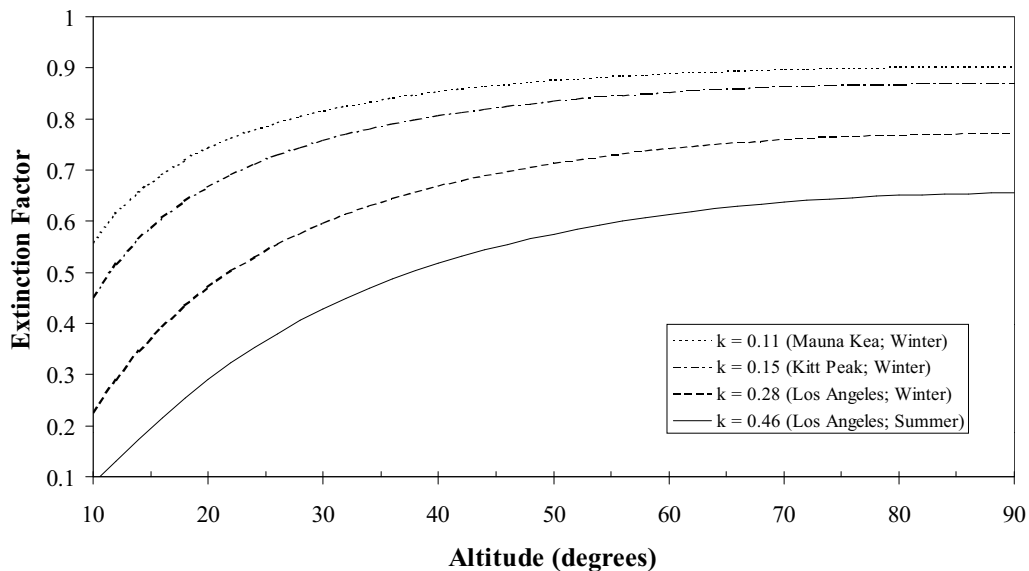

Figure 4.32: Behaviour of extinction factor Ext with altitude. The effect of air quality in an urban environment (Los Angeles) is also shown for comparison.

For a given bandwidth of $\Delta\lambda$ nanometres, the power incident on the telescope objective is then obtained from equations (4.77), (4.78) and (4.79) to give:

$$P_{tel} = I_{deb}\, \Omega_{tel}\, \text{Ext}\, \Delta\lambda \quad \text{(W).} \tag{4.80}$$

4.14.1.2   Optics transmission

By far the biggest factor affecting light transmission through the telescope is the central obstruction provided by the secondary mirror. In Schmidt-Cassegrain telescopes (SCTs) of large diameter, the secondary diameter is typically 30% that of the primary, i.e. a transmission factor of 91%.

The transmission factors of the two mirrors and corrector plate of the SCT are each of the order of 99%, so that transmission is $0.99^3 = 0.97$.

The Detector Quantum Efficiency (DQE) of a CCD is a measure of the ability of a CCD to detect every photon that falls on it. No CCD at the present time can detect every photon (a DQE of 100%), but by using fluorescent dyes and/or chip thinning the DQE of CCDs can be raised to above 50% in the visible region. For a wavelength of 550nm, the DQE of a typical CCD is about 60% (Lobb and Dick, 1992, p23).

Total transmission ρ due to the above three factors therefore amounts to

$$\rho = 0.91 \times 0.97 \times 0.60 = 0.53. \tag{4.81}$$

4.14.1.3   Plate Scale

The plate scale is the factor that relates angular separation in the sky to linear measure in the focal plane. The displacement x in the focal plane is caused by an object subtending an angle θ such that:

$$\tan \theta = \frac{x}{f} \quad \Rightarrow \quad \theta \approx \frac{x}{f} \text{ for small angles,} \tag{4.82}$$

where f = focal length of telescope, so that x takes the same units as f. Therefore using the appropriate units, the plate scale can be defined as:

$$s_p = \frac{\theta}{x} = \frac{1}{f} \text{ arcsec/mm.} \tag{4.83}$$

4.14.1.4   Streak Image Dimensions

In the absence of a turbulent atmosphere, a point source on the sky is not imaged to a single point in the focal plane because of Fraunhofer diffraction at the primary aperture. Rather, the energy is spread out in a pattern described by the Airy function,

$$I_\theta = I_o \left[\frac{2J_1(a)}{a} \right]^2 , \qquad (4.84)$$

where $I_{\theta,o}$ = normalised intensity at angle θ and at the optical axis respectively, J_1 = Bessel function of the 1st order, and a is given by:

$$a = \frac{\pi D \sin \theta}{\lambda} = \frac{\pi D \theta}{\lambda} , \qquad (4.85)$$

where D = telescope objective diameter, λ = observing wavelength. The resulting intensity pattern in the focal plane is shown in Figure 4.33.

Due to turbulence in the atmosphere however, the image is blurred such that fine detail of the Bessel function is lost and the image is spread into an area ~1–2" wide, and for this reason the central peak of the shape is often approximated by a gaussian curve of order:

$$I_a = I_o \exp\left(\frac{-a^2}{2\sigma^2} \right) , \qquad (4.86)$$

which is illustrated to a different scale in Figure 4.34.

The "seeing" of the atmosphere is taken to be the Full Width at Half Maximum (FWHM) of the gaussian curve, therefore by setting I_a to $I_o/2$ in (4.86) the seeing is related to σ by:

$$\text{seeing} = 1.177\sigma. \qquad (4.87)$$

Now, the finite integration time coupled with the topocentric angular speed means that the debris image will streak on the CCD frame. To facilitate the area calculation, the gaussian curve is approximated to a top hat function of equal volume and height (Figure 4.35). Appendix 2 shows the calculation of the top hat function (or "spot") dimensions in detail, but the main result is that the radius of the spot is given by:

$$r_s = \sigma\sqrt{2} . \qquad (4.88)$$

From equation (4.87) the radius of the top hat spot is related to the seeing therefore by:

$$r_s = 1.202 \times \text{seeing}. \qquad (4.89)$$

The streak width is therefore the diameter of the spot ($d_s = 2\, r_s$), and its length the product of the topocentric angular speed ω_{top}, the integration time τ, and the plate scale s_p, giving an area of:

$$A_{streak} = d_s \, \omega_{top} \, \tau \, s_p \quad \text{pixels.} \tag{4.90}$$
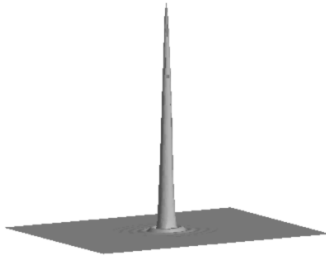
Figure 4.33: Qualitative representation of the Airy pattern of the debris image. The central peak out to the first minimum, known as the "Airy Disk" which contains 84% of the total flux, has a diameter of approximately 0.3" for a 1 metre telescope .
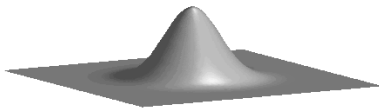
Figure 4.34: Atmospheric turbulence spreads the ideal Airy pattern out into a shape that is often approximated to a gaussian, with a base diameter of the order of 1-2".
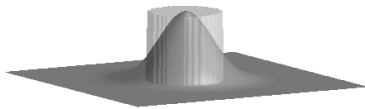
Figure 4.35: The gaussian may be approximated to that of a top hat function of equal height and volume.

The energy of a photon is given by:

$$E_{phot} = \frac{h \, c}{\lambda} \quad \text{(J)}, \tag{4.91}$$

where h = Planck's constant (6.6262×10^{-34} J s), c = speed of light in vacuum (2.9979×10^{8} m s^{-1}). Therefore the energy of each photon at the operating wavelength of 550nm is:

$$E_{phot} = 3.6118 \times 10^{-19} \quad \text{J.} \tag{4.92}$$

The flux of photons per second at the telescope objective is therefore:

$$\text{Flux}_{tel} = \frac{P_{tel}}{E_{phot}} \quad \text{photons s}^{-1}. \tag{4.93}$$

After transmission losses through the telescope optics, and further losses in the conversion from photon to electron at the CCD (all encompassed by the transmission factor ρ), the total number of electrons produced during the integration time τ over the entire streaked debris image (the streak signal S_{streak}) is given by:

$$S_{streak} = \text{Flux}_{tel} \, \tau \, \rho \quad \text{electrons.} \tag{4.94}$$

So that the total count per pixel, which is the debris signal (S_{deb}), is:

$$S_{deb} = \frac{S_{streak}}{A_{streak}} = \frac{P_{tel}\,\tau\,\rho}{E_{phot}\,A_{streak}} \quad \text{electrons.} \tag{4.95}$$

4.14.1.5   Penumbra Shading

The fraction of unobscured solar disk is calculated following the equations given in section 4.7, if the solar disk is partially covered by the Earth's horizon. The result is a factor ("PenFactor"), calculated separately, which is simply multiplied by the debris signal S_{deb}.

4.14.2 Galactic and Ecliptic Background

The contribution to the background sky from the galactic plane and zodiacal light is calculated according to the routines specified in sections 4.11 and 4.12 respectively. The units of brightness were specified in terms of S_{10}, i.e. the flux equivalent to the number of 10th-magnitude stars per square degree. These fluxes are converted into electron counts at the CCD by first converting the S_{10} value to a photon flux at the top of the atmosphere:

$$F_{S_{10}} = \frac{S_{10} \cdot F_{10}^{*}}{k_a \cdot E_{ph}} \quad \text{(photons s}^{-1}\text{ m}^{-2}\text{nm}^{-1}\text{arcsec}^{-2}), \tag{4.96}$$

where: S_{10} = sky brightness in question; F_{10}^{*} = flux of 10th magnitude star in visible band (3.44×10^{-15} Wm^{-2}nm^{-1}); k_a = number of square arcseconds in one square degree (1.296×10^{7}); E_{ph} = energy of one photon at 650nm (3.056×10^{-19} J).

4.14.3 Night Sky Contribution

This is calculated in the same manner as the galactic and zodiacal brightness above, with the exception that the airmass extinction factor is omitted. The value of sky brightness is taken to be a constant with a value of 21.9 magnitudes per square arcsecond (5.98×10^{-20} W m^{-2} nm^{-1} arcsec^{-2}) (Benn & Ellison, 1998).

4.14.4 Scattered Moonlight Contribution

The value B_{moon} (nL) is calculated according to routines specified in section 4.10.1. An equivalence of the nanoLambert unit is quoted in Schaefer (1993) as 1nL = 26.33 magnitudes arcsec^{-2}, which is equivalent to 1.01×10^{-21} W m^{-2} nm^{-1}

arcsec^{-2}. This is converted to a photon flux by dividing by the energy of one photon, as in section 4.14.2.

4.14.5 Readout Noise Contribution

CCD readout noise is taken as a constant with a value of 10 electrons per pixel, as the program simulates the ESA Concept A telescope, for which the CCDs have such a readout noise value (Lobb and Dick, 1992).

4.15 Summary

- The SkyPlot program uses some techniques designed to optimise it for speed, sacrificing complexity. These procedures were more necessary in the past than they are now, but nevertheless they remain in the code as there would be no detrimental effect on computing speed.
- Equations of satellite and observer motion that are utilised in the program are presented.
- Physical effects taken into account include: Earth oblateness perturbations (to J_2); Refraction and Earth oblateness effects on true alt/azimuth measurements for the observer; the shadow of the Earth including contribution from the penumbra; the apparent motion of the Sun and Moon; brightness of the night sky background including contributions from the Milky Way and Zodiacal Light; and finally, details of the Signal-to-Noise calculation performed by the program are discussed in detail.
- The full code listing of the SkyPlot program is given in Appendix 3.